Influence of Vanadium Pentoxide Addition on the Structural and Electromagnetic Properties of Li-Zn Ferrites

by

Sm. Rubayatul Islam

MASTER OF SCIENCE IN PHYSICS

Department of Physics

BANGLADESH UNIVERSITY OF ENGINEERING AND TECHNOLOGY

October 2021

The thesis titled "Influence of Vanadium Pentoxide Addition on the Structural and Electromagnetic Properties of Li-Zn Ferrites" Submitted by Sm. Rubayatul Islam, Roll No. 1018142502F, Session: October/2018, has been accepted as satisfactory in partial fulfillment of the requirement for the degree of MASTER OF SCIENCE IN PHYSICS on 09 October 2021.

BOARD OF EXAMINERS

1. **Dr. Muhammad Samir Ullah**   Chairman
   (Supervisor)
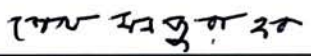   Associate Professor
   Department of Physics, BUET, Dhaka-1000

2. **Dr. Md. Rafi Uddin**   Member
   Professor and Head   (Ex-officio)
   Department of Physics, BUET, Dhaka-1000

3. **Dr. A. K. M. Akther Hossain**   Member
   Professor
   Department of Physics, BUET, Dhaka-1000

4. **Dr. Mohammad Khurshed Alam**   Member
   Associate Professor
   Department of Physics, BUET, Dhaka-1000
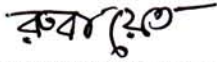
5. **Dr. Eng. Sheikh Manjura Hoque**   Member
   Chief Scientific Officer & Head   (External)
   Material Science Division, Atomic Energy Centre,
   Dhaka-1000, Bangladesh

CANDIDATE'S DECLARATION

It is hereby declared that this thesis or any part of it has not been submitted elsewhere for the award of any degree or diploma.

রুবায়েত

....

Sm. Rubayatul Islam

DEDICATED

To

"My beloved parents"

Acknowledgments

Abstract

The influence of V_2O_5 addition on the microstructural, electrical and magnetic properties of Li-Zn ferrites having the compositions $Li_{0.25}Zn_{0.50}Fe_{2.25}O_4 + xV_2O_5$ (where x = 0.0, 0.4, 0.8 and 1.2 wt %) are reported in this study, where the samples are sintered at 1050 °C. The X-ray diffraction patterns confirmed that the crystal structures of all the prepared samples were the cubic spinel phase. Microstructural studies showed that the average grain sizes were increased from 5.3 (for x = 0.0 wt%) to 7.7μm (for x = 0.8 wt% V_2O_5), which could be attributed to the role of V_2O_5 as sintering aid to enhance the densification of the samples. The magnetic hysteresis analysis demonstrated that the saturation magnetizations were increased from 44.0 (for x = 0.0 wt%) to 50.3 emu/g (for x = 0.8 wt% V_2O_5). However, the saturation magnetization was found to decrease for x = 1.2 wt% V_2O_5, which may be related to weaken of exchange interaction due to the introduction of excess non-magnetic V_2O_5. The complex initial magnetic permeability has been studied, and it shows that the enhancement of the permeability is clearly evidenced on V_2O_5 addition. The complex impedance spectroscopy through Cole-Cole plot has demonstrated a partial semicircular arc, which indicates that the conduction mechanism takes place predominantly through the grain property.

Contents

List of Figures

List of Tables

List of Abbreviations

XRD	X-ray Diffraction
$F(\theta)$	Nelson-Riley function
D	Average grain size
FESEM	Field Emission Scanning Electron Microscopy
EDS	Energy Dispersion Spectroscopy
AC	Alternating current
B	Magnetic induction
H	Magnetic field
f_r	Resonance frequency
J	Exchange integral
K	Total anisotropy
L_s	Self-inductance of the sample core
L_o	Inductance of the winding coil without sample
μ_i^*	Complex initial permeability
ε^*	Complex dielectric constant
M	Magnetization
M_s	Saturation magnetization
H_c	Coercivity
N_A	Avogadro's number
P	Porosity
ρ_B	Bulk density
RQF	Relative Quality factor
T_c	Curie temperature
T_s	Sintering temperature
Z	Complex impedance
M_w	Molecular weight

CHAPTER 1

INTRODUCTION

1.1 Spinel Ferrites

Spinel ferrites are magnetic oxide materials which have been commercially used in electronic and telecommunication industries due to their noteworthy properties such as mechanical hardness, chemical stability, large magnetic induction, moderate saturation magnetization, high electrical resistivity and low dielectric loss etc. [1-5]. Ferrites are ferrimagnetic materials which consist of double oxides of iron and another metal oxide. The general chemical formula of the ferrite is MFe_2O_4, where M is denoted a divalent metal ion such as Fe^{2+}, Co^{2+}, Mn^{2+}, Ni^{2+}, Cu^{2+}, Zn^{2+}, Mg^{2+} or Cd^{2+}. There are different types of spinel ferrites such as normal, inverse and mixed spinel ferrites. The arrangement of the form $(M_xFe_{1-x})_A[M_{1-x}Fe_{1+x}]_BO_4$ is often referred as mixed spinel, where the first term within the first bracket indicates the tetrahedral sites and the second term within the square bracket indicates the octahedral sites [6]. (i) When x = 1, it is called normal spinel. In this type of ferrites, the divalent metal ions occupy in A-sites and the trivalent ions occupy in B-sites. $ZnFe_2O_4$ and $CdFe_2O_4$ are the examples of normal spinel ferrites. (ii) When x= 0, it is called inverse spinel type and $Li_{0.5}Fe_{2.5}O_4$, $CoFe_2O_4$, $CuFe_2O_4$ are the inverse spinel ferrites. In this ferrite, one trivalent Fe^{3+} is at the tetrahedral or A sites, while the remaining trivalent Fe^{3+} and the divalent metallic ions M^{2+} are at the B sites.

1.2 Motivation

Soft spinel ferrites are one of the important ferrimagnetic materials due to their extensive applications with electronic industries [7-9]. Lithium ferrite ($Li_{0.5}Fe_{2.5}O_4$) emerges as a good microwave material owing to its high Neel (T_N) temperature, low magnetic losses, superior temperature stability of saturation magnetization, and low eddy current losses, etc. [10-14]. Moreover, polycrystalline lithium-zinc (Li-Zn) ferrites are promising materials which have been widely used in electronic industries as well as telecommunication technology owing to their significant properties such as high magnetic permeability, high dielectric constant, wider band absorption frequency region, high electrical resistivity, high mechanical strength, and low dielectric loss [15-20]. The electrical and magnetic properties of ferrites are dependent on various parameters such as the preparation techniques, cation distribution, sintering

temperatures, types and amount of elemental substitution or addition [21-23]. An additive may play a significant role to improve the mass transport mechanism due to the presence of the liquid phase at the sintering process. Previously, various types of additive oxides such as V_2O_5, SiO_2, MnO_2, MoO_3, Nb_2O_5 and Bi_2O_3 were used as an additive to influence the microstructure and magnetic properties of the spinel ferrites. Xu et al. [24] studied the investigation of grain growth and magnetic properties of Li-Zn-Ti ferrites. They observed that the compactness of Li-Zn-Ti ferrites strongly depended on V_2O_5 addition. Liu et al. [25] observed the effect of sintering temperature on microstructure and magnetic properties of Li-Zn ferrites with Bi_2O_3 addition. They found that the densification and grain growth rate were notably improved by the amount of Bi_2O_3 additive. Lebourgeois et al. [26] investigated the effect of V_2O_5 addition on the magnetic properties and morphological behaviors of Ni-Cu-Zn ferrites. They found that the densification and microstructure of Ni-Cu-Zn ferrites are strongly depended on the amount of V_2O_5. Mahmoudi et al. [27] studied temperature and frequency dependence of electromagnetic properties of Li-Zn ferrites with nano-SiO_2 additive. It revealed that the nano-SiO_2 played a significant role for the modification of electrical and magnetic properties. Wang et al. [28] studied the V_2O_5-doped Ni-Cu-Zn ferrites and they found uniform grains at low-sintering temperature which modify the magnetic properties. The results exhibited that the introduction of V_2O_5 promoted grain growth, reduction of porosity and obtained a denser microstructure of Ni-Cu-Zn ferrites. Mirzaee et al. [29] observed the influence of V_2O_5 as an effective dopant on the development of microstructure and magnetic properties of Ni-Zn ferrites. They found that the permeability and relative density were increased with the amount of V_2O_5 up to 1.6 wt%. Janghorban et al. [30] studied the influence of V_2O_5 addition on the grain growth and magnetic properties of Mn-Zn high permeability ferrites. They observed that the permeability of Mn-Zn ferrites were increased due to a small amount of additive V_2O_5 content, but it decreases for the higher amount of V_2O_5 additive.

Usually, spinel ferrites are required high sintering temperature in order to obtain homogeneous and densification of the materials. However, abnormal grain growth or discontinuous grain growth appears at the high sintering temperature, which can deteriorate the electromagnetic properties of the spinel ferrites [31, 32]. In order to obtain pore free with homogeneous grain and faster densification of Li-Zn ferrites, V_2O_5 can play a role as the sintering aid that promotes to grain growth of the ferrites due to

the liquid phase (melting temperature ~ 690 °C) in the sintering process [33-35]. On the other hand, several methods such as hydrothermal process, co-precipitation method, electro-spinning method, sol-gel self-ignition technology and conventional solid state reaction method are often used to synthesize spinel ferrites. Among them, solid state reaction technique is easier and convenient than other methods due to the availability of raw materials, easier synthesized route and ability to improve the homogeneity of the samples [36, 37]. The high magnetic permeability also plays a crucial role in magnetic softening of the spinel ferrites from the application of point views. In this regard, it is expected that V_2O_5 can play a significant role as the sintering aids in order to improve the mass transport mechanism and densification of the Li-Zn ferrites samples. V_2O_5 additive can also reduce the sintering temperature of the ferrites sample due to increase in grain growth in the samples. Gao *et al.* [10] studied the electromagnetic and microwave absorption properties of Ti-doped Li-Zn ferrites having the compositions $Li_{0.25+x/2}Zn_{0.50}Fe_{2.25-x}Ti_{2x/3}O_4$. They have shown that the initial permeability increases with the increase of Li and Ti contents which could be attributed to the decline in anisotropy constant of the samples. On the other hand, the saturation magnetization of $Li_{0.25}Zn_{0.50}Fe_{2.25}O_4$ was found to larger in compared to other samples. In this regard, the sample with $Li_{0.25}Zn_{0.50}Fe_{2.25}O_4$ composition has been chosen based on the magnetic properties. Therefore, it is expected that the addition of V_2O_5 would tailor the microstructural and the electromagnetic properties of Li-Zn ferrites. So far, there is inadequate data available on the structural, electrical, magnetic and microstructural properties of Li-Zn ferrites with the addition of V_2O_5. In the present study, a detailed study has been carried out to examine the effect of V_2O_5 addition on structural and electromagnetic properties of $Li_{0.25}Zn_{0.50}Fe_{2.25}O_4$ using the conventional solid state reaction technique.

1.3 Objectives of the Present Study

The objectives of this research study are

(i)   Preparation of $Li_{0.25}Zn_{0.50}Fe_{2.25}O_4 + xV_2O_5$ (where $x = 0.0, 0.4, 0.8,$ and 1.2 wt%) compositions using standard solid state reaction method.

(ii)   Observation of the crystal structure of the prepared samples using an X-ray diffraction technique.

(iii)   Investigation of the surface morphology and compositional analyses using Field Emission Scanning Electron Microscopy and Energy Dispersive X-ray, respectively.

(iv)   Observation of the magnetic hysteresis curve at room temperature for various compositions.

(v)   Investigation of the complex magnetic permeability and the relative quality factor (RQF) as a function of frequency at room temperature for all the samples.

(vi)   Measurement of the relative dielectric constant and dielectric loss factor as a function of frequency at room temperature.

(vii)   Investigation of the variation of the ac electrical conductivity with applied function for all the prepared samples.

(viii) Observation of the impedance spectroscopy for all the samples.

1.4 Outline of the Thesis

The organization of this thesis is as follows:

Chapter-1 deals with the importance of spinel ferrites, motivation of the research and objectives of the present work.

Chapter-2 gives literature review of earlier research, structure of the spinel ferrite and theoretical backgrounds.

Chapter-3 gives the details of the sample preparation, describes the experimental part and descriptions of different measurement techniques that have been used in this research work.

Chapter-4 shows the results and discussion for various investigations in this research study.

Chapter-5 represents the summary and conclusions of the overall experimental results.

CHAPTER 2

LITERATURE REVIEW AND THEORETICAL ASPECTS

2.1 Literature Review

Many researchers have studied on structural, surface morphology, magnetic and electrical properties of Li-Zn ferrites for the significant applications in electronic and telecommunication technology. These are discussed as follows:

Gao *et al.* [10] studied the structural, electromagnetic and microwave absorption properties of Ti doped Li-Zn ferrites having formula $Li_{0.23+x/3}Zn_{0.5}Fe_{2.25-x}Ti_{2x/3}O_4$ (where x = 0.0, 0.3, 0.6, 0.9). The study of X- ray photoelectron spectroscopy (XPS) revealed that the concentration of Fe^{2+} ions and oxygen vacancies in the samples increased with Li and Ti contents. The wide range of Curie temperatures were found from 56 to 301 $^\circ$C for this study. The saturation magnetization was found to be maximum, while the coercivity was minimum for x = 0.0. Then the saturation magnetization decreased monotonically with the increase of Li and Ti contents. They also found that the initial permeability and dielectric constant were maximum at x = 0.9 content. The value of bandwidth was found to be 6.2 GHz under -10 dB and minimum reflection loss obtained at 18.87 dB.

Singh *et al.* [11] investigated the dielectric relaxation, conductivity behavior and magnetic properties of Mg substituted Zn-Li ferrites. They prepared different compositions of series $Zn_{0.5}Li_{1-2x}Mg_xFe_2O_4$ ($0 \leq x \leq 0.5$) by sol-gel auto combustion technique. They observed that dielectric constant (ϵ') and dielectric loss factor (tanδ) decreased with the applied frequency and it increases with the increase in temperature. Again ϵ' and tanδ were found to be maximum at x = 0.5 and minimum at x= 0, respectively. Conductivity becomes constant in the low frequency region and showed dispersion in the high frequency region. The semiconducting nature of the samples is demonstrated by the linear variation of conductivity with temperature. The mechanism of electrical conduction and dielectric relaxation were identical in a consequence of nearly similar values of activation energy for dc conduction and for conductivity relaxation, and suggesting a non-Debye type relaxation process. The results of magnetic properties of these ferrites suggested the super paramagnetic behavior due to the absence of hysteresis and non-attainment of saturation magnetization (even at 8 kOe).

Rathod *et al.* [12] studied the effect of Zn-substitution on the structural and magnetic properties of Li-ferrite powders with the formula $Li_{0.5-x/2}Zn_xFe_{2.5-x/2}O_4$; x = 0.0, 0.2, 0.4, 0.6, 0.8 and 1.0. The Rietveld refinement of the XRD data confirmed the preferential occupancy of the Zn-atoms at the tetrahedral sites and the Li atoms at the octahedral sites of the spinel structure. Trace amounts of zinc-oxide and iron-oxide impurity phases were found for the samples with high Zn content (x ≥ 0.6). Fourier transform infrared (FTIR) spectroscopy confirmed the presence of broad absorption bands between tetrahedral and octahedral site in the spinel structure of the Li-Zn ferrites. The saturation magnetization of the samples reduced with the substitution of higher amount of Zn^{2+} ions content.

Fazio *et al.* [13] investigated the electromagnetic properties of Mn-Zn ferrite with lithium substitution. The composition of $Li_{0.5x}Mn_{0.4}Zn_{(0.6-x)}Fe_{2+0.5x}O_4$ was prepared by the ceramic method. The doping of lithium influenced the saturation magnetization as its value varied from 57.5 emu/g for x = 0.0 to 82.9 emu/g for x = 0.4 having the content of maximum real permeability. The sample has maximum resistivity (4.4×10^7 Ω cm) and minimum dielectric constant with higher Li content. The inclusion of lithium enhanced microwave absorption with a maximum reflection loss of 45 dB at 140 MHz. These modified Li-Zn ferrites exhibited good electromagnetic properties in the microwave range of 1MHz-1GHz used as absorbers.

Anupama *et al.* [14] observed the composition dependent elastic and thermal properties of Li-Zn ferrites. The chemical composition of $Li_{0.5-x/2}Zn_xFe_{2.5-x/2}O_4$ (where x = 0.0, 0.2, 0.4, 0.6, 0.8 and 1.0) ceramics were synthesized by the auto combustion method. The IR absorption frequencies, the lattice parameters and the mass-densities were used to evaluate the elastic and thermal parameters such as force constant, elastic moduli and Debye temperature of the studied Li-Zn ferrite samples was observed as a function of Zn-content x. The force constants of the octahedral site complexes and tetrahedral site complexes, and elastic moduli were increased with increasing Zn content (maximum at x = 1.0). In order to stronger interaction between cation and anions, the high elastic moduli and Debye temperature of the samples provided the stiff nature of Li-Zn ferrite particles. The calculated Debye temperature (θ_D) was almost similar to the values of literature obtained with experimental result.

Additive plays an important role in order to modify the electromagnetic properties of the spinel ferrite. There are different types of additive such as V_2O_5, Nb_2O_3, MoO_3 and Bi_2O_3 which have been used as the sintered aid in order to modify the microstructural, electrical and magnetic properties of the spinel ferrites. These are discussed as below:

Xu *et al.* [24] studied the investigation of grain growth and magnetic properties of low sintered Li-Zn-Ti ferrite-ceramic with the addition of V_2O_5. The compositions of $Li_{0.43}Zn_{0.27}Ti_{0.13}Fe_{2.17}O_4 + xV_2O_5$ (having x = 0.00, 0.10, 0.20, 0.40, 0.60 and 0.80 wt%) were prepared with the solid state reaction method. In this study, the Li-Ti-Zn ferrite-ceramic sintered at 925 ºC produced dense microstructure using the synthesis process of solid state reaction technique. They investigated that the average grain size, high saturation flux density (B_s) and high saturation magnetization of the samples were found to be 6.38 μm, 324.4 mT and 4277 gauss, respectively for the amount of 0.4 wt% V_2O_5. The coercivity decreased with the addition of V_2O_5 content, which indicates the magnetic softness nature of the samples.

Liu *et al.* [25] observed the effects of sintering temperature on microstructure and magnetic properties of Li-Zn ferrites with Bi_2O_3 content. The ferrites with composition $Li_{0.35}Zn_{0.3}Fe_{2.35}O_4 + x\ Bi_2O_3$ (x = 0.0 to 3.0 wt% with an interval 0.5) were prepared by conventional ceramic method. They found that the densification behavior and grain growth rate were notably improved by the addition of Bi_2O_3 which exhibited liquid phase characteristics due to low melting point (825 ºC). The porosity was reduced at 1.0 wt% Bi_2O_3 content and then porosity increased with increasing of additive contents. For the sample with 1.0 wt% Bi_2O_3 additive, a high saturation magnetization, squareness ratio, minimum ferromagnetic resonance line-width and low coercive were investigated with sintered at 1100 ºC. Moreover, the squareness ratio decreased when Bi_2O_3 content was beyond 1.0 wt%, which was caused by higher porosity located either in grains or at grain boundaries.

Lebourgeois *et al.* [26] observed the influence of V_2O_5 addition on the magnetic properties of Ni-Zn-Cu ferrites. The ferrite samples $Ni_{0.24}Zn_{0.55}Cu_{0.2}Co_{0.02}Fe_{1.99}O_4$ synthesized by solid state reaction for sintering temperature of 850 and 1000 ºC. The density of the ferrite increased upto 5.14 g/cm^3 for 1 wt% V_2O_5 and then slightly decreased at the sintering temperature 850 ºC. It was observed that the magnetic properties were deteriorated for the content higher than that of 0.6 wt% V_2O_5. The

micro structural property improved with the tuning of the sintering range. The complex permeability of ferrite samples with toroid shaped was measured by impedance analyzer from 1MHz to 1.8GHz. The magnetic permeability was decreased due to the various defects in the grain. This defect came from the domain walls and pores in the sample, and then declined to permeability.

Wang *et al.* [28] synthesized the V_2O_5-doped Ni-Cu-Zn ferrites in low-sintered with uniform grains and enhanced magnetic properties. The compositions of $(Ni_{0.2}Cu_{0.2}Zn_{0.6})_{1.03}(Fe_2O_3)_{0.97}$ with different contents of V_2O_5 (0.00, 0.25, 0.50 and 0.75 wt%) were prepared by solid-state reaction technique within low sintering temperature. The XRD patterns ensured that adding a small amount of V_2O_5 could not influence the formation of the spinel phase polycrystalline Ni-Cu-Zn ferrites. The results exhibited that the introduction of V_2O_5 promoted grain growth, reduced porosity and obtained a denser microstructure of Ni-Cu-Zn ferrites. The density increased with increasing of V_2O_5 contents up to 0.50 wt% then slightly decreased for 0.75 wt% content. They found high permeability, high saturation magnetic flux density, high remanence, high Q-value, and low coercivity when the samples were sintered at 900 ºC. When adding excessive amount of V_2O_5 content, the grain uniformity deteriorated results the magnetic properties went down.

Mirzaee *et al.* [29] observed the influence of V_2O_5 as an effective dopant on the microstructure development and magnetic properties of $Ni_{0.64}Zn_{0.36}Fe_2O_4$. V_2O_5-added $Ni_{0.64}Zn_{0.36}Fe_2O_4$ with different compositions was prepared using standard solid state reaction method. They found that the permeability and relative density were increased with increasing the amount of V_2O_5 up to 1.6 wt% and then decreased. The specific resistivity of the samples increases continuously. T_c were found to be maximum for 0.8 wt% V_2O_5 content and saturation magnetization shows peak value at 1.2 wt% of V_2O_5.. The average grain size was larger at 1.6 wt% V_2O_5 in compare to other compositions.

Janghorban *et al.* [30] studied the influence of V_2O_5 addition on the grain growth and magnetic properties of Mn-Zn ferrites. The samples were prepared by solid state reaction method with V_2O_5 contents (0.0 to 3.0 wt%). This observation found that the permeability of Mn-Zn ferrites was increased for a small amount of V_2O_5 additive, while it was decreased for the higher amounts of additive. The Curie temperature and saturation magnetization were increased by V_2O_5 additive in a certain weight percentage

and then it decreased. At low concentration of V_2O_5, the magnetic permeability was increased by about 42% than that of pure Mn-Zn ferrites.

Rao *et al.* [38] studied the complex permeability spectra of Ni-Zn ferrites doped with V_2O_5/Nb_2O_5. They prepared the samples with the conventional ceramic method. The sample with V_2O_5 additive was sintered at 1210 ^{o}C, whereas the sample with Nb_2O_5 was sintered at 1250 ^{o}C. It was found that the microstructures of Nb_2O_5 added samples at lower concentration did not promote the grain growth for sintering temperature of 1250°C, while the microstructure at higher concentration reveals larger grain growth. On the other hand, the vanadium doped in Ni-Zn ferrites show high densities due to lower melting point of V_2O_5. It was also found that the complex magnetic permeability spectra of these ferrites have shown the frequency stability up to a few MHz.

The influence of MoO_3 and V_2O_5 co-doping on the magnetic and microstructural properties of Ni-Zn ferrite were observed by Mirazaee *et al.* [39]. The ferrites were prepared by the conventional powder method with sintered 1100 ^{o}C. In this study, they were used Fe_2O_3, ZnO, NiO, V_2O_5 and MoO_3 as the raw materials to prepare of ferrites. The compositions were sintered at different temperatures. It was found that the samples doped with V_2O_5 and MoO_3 have shown lower power loss in compare to pure Ni-Zn spinel ferrites. The small addition of MoO_3 and V_2O_5 increased density about 8% and promoted average grain size about 5 times than the ferrites without doping. They investigated the promotion of real permeability along with saturation magnetization and reduced power loss due to the additives.

2.2 Theoretical Aspects

2.2.1 Ferrites

Ferrites have the cubic structure, which is very close to mineral spinel $MgO.Al_2O_3$ and are called cubic spinel. Analogous to the mineral spinel, magnetic spinel have the general formula, $MeO.Fe_2O_3$ or $MeFe_2O_4$, where Me is the divalent metal ion [40]. The structure was first determined by Bragg and Nishikawa [41-42]. Formerly, spinel's containing Fe were called ferrites, but now the term has been broadened to include many other ferrimagnetism including garnets and hexagonal ferrites and these need not necessarily contain iron. In the ideal spinel structure the anions form cubic close packing, in which the cations partly occupy the tetrahedral (A-sites) and octahedral (B-sites) interstices. Fig. 2.1 shows the lattice structure of spinel ferrite.
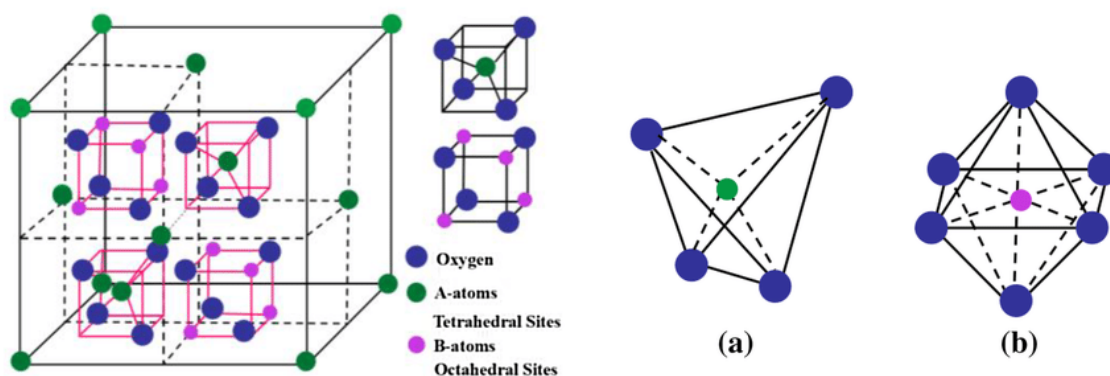
Fig. 2.1 The unit cell structure of spinel ferrite.

Now, the interstices are not all the same: some which we call A-sites are surrounded by or coordinated with 4 nearest neighboring oxygen ions whose lines connecting their centers form a tetrahedron. Thus, A-sites are called tetrahedral sites. The other types of B-sites are coordinated by 6 neighboring oxygen ions whose lines connecting their centers form an octahedron. Thus B-sites are called octahedral sites. In the unit cell of 32 oxygen ions there are 64 tetrahedral sites and 32 octahedral sites. It turns out that of the 64 tetrahedral sites, only 8 are occupied and out of 32 octahedral sites, only 16 are occupied. Thus structure of spinel compounds is complex; the unit cell contains 8 formula units AB_2O_4, with 8 A-sites, 16 B-sites and 32 oxygen ions, and total of $8\times7 = 56$ ions. A spinel unit cell contains two types of sub cells, the two types of sub cells alternate in a three dimensional array so that each fully repeating unit cell requires 8 sub

cells. The positions of the ions in the spinel lattice are not perfectly regular and some distortion does occur .The tetrahedral sites are often too small for the metal ions so that the oxygen ions move slightly to accommodate them. The oxygen ions connected with the octahedral sites move in such a way as to shrink the size the octahedral cell by the same amount as the tetrahedral site expands. The movement of the tetrahedral oxygen is reflected in a quantity called the oxygen parameter, which is the distance between the oxygen ion and the face of the cube edge along the cube diagonal of the spinel sub-cell. This distance is theoretically equal to $3/8a$, where 'a' is the lattice constant. In spinel structure the distribution of cations over the tetrahedral or A sites and octahedral or B sites can be present in a variety of ways. If all the Me^{2+} ions in $Me^{2+} Me_2^{3+}O_4$ are in tetrahedral and all Me^{3+} ions in octahedral positions, the spinel is then called normal spinel. Another cation distribution in spinel exists, where one half of the cations Me^{3+} are in the A-sites and the rest, together with the Me^{2+} ions are randomly distributed among the B-sites.

The spinel having the latter kind of cation distribution is known as inverse spinel [43].

i) Normal Spinel: divalent metal ions are on A sites: $Me^{2+} [Me_2^{3+}] O_4$

ii) Inverse Spinel: divalent metal ions are on B sites: $Me^{3+} [Me^{2+}Me_2^{3+}] O_4$

A completely normal or inverse spinel represents the extreme cases; Zn-ferrites have normal spinel structure. On the other hand, Li-ferrites have inverse spinel structure. There are many spinel oxides which have cation distributions intermediate between these two extreme cases and are called mixed spinel. The general cation distribution for the mixed spinel ferrites can be written as: $(Me_x^{2+}Me_{1-x}^{3+})[Me_{1-x}^{2+}Me_{1+x}^{3+}]O_4^{2-}$ where the first and third brackets represent the A and B sites, respectively.

2.2.2 Exchange interaction in the spinel ferrites.

Spontaneous magnetization of spinel ferrites can be obtained on the basis of their composition, cation distribution and the relative strength of the possible interaction. The super exchange interaction of the spinel ferrites are strongly depended on the tetrahedral (A) and octahedral (B) sites. The strongest super exchange interaction is expected to occur between octahedral and tetrahedral cations. The strength of interaction or exchange force between the moments of the two metals ions on different sites depends (i) on the distances between these ions and the oxygen ion that links them and (ii) on the

angle between the three ions. The interaction is greatest for an angle of 180°, where the interionic distances are the shortest. In the A-A and B-B cases, the angels are too small or the distances between the metal ions and the oxygen ions are too large. The best combination of distances and angles are seen in A-B interactions. For an undistorted spinel, the A-O-B angles are about 125° and 154°. The B-O-B angles are 90° and 125° but the latter, one of the B-B distances is large. In the A-A case the angle is about 80°. Therefore, the interaction between A and B sites is strongest. The B-B interaction is much weaker and the most unfavorable situation occurs in the A-A interaction. The super-exchange cationic interactions are denoted by J_{AB}, J_{AA} and J_{BB} which are modified by introducing cationic substitutes with different valence states, radii or magnetic moments in either or both of the A and B sub-lattices [44].
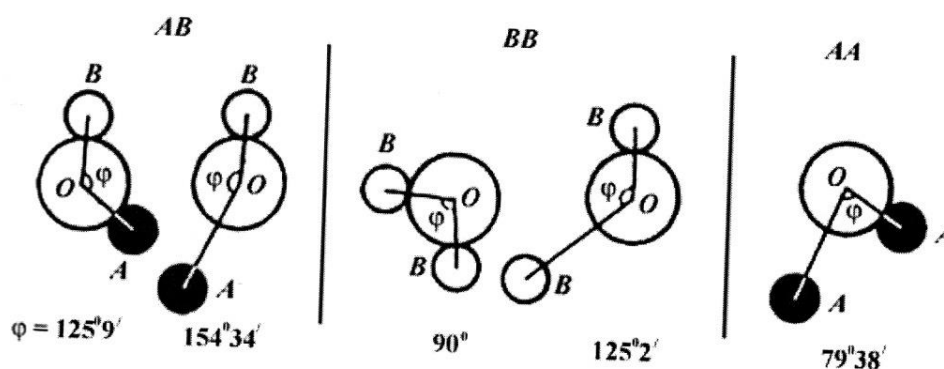
Fig. 2.2 Inter ionic angles for the different type of lattice site interactions [45].

2.2.3 Hysteresis loop

The state of magnetization of a solid is a function of the strength and direction of the magnetizing field. If we consider a ferromagnetic material which contains many small magnetic domains but no net magnetization, we can examine what happens to the domains as the field strength is increased. As the field is increased from zero, the effect on the solid is to displace domain boundaries in a reversible fashion. If the magnetic field is switched off, the domain boundaries return to their starting positions. Thus the initial part of the B-H curve results from reversible domain boundary displacement and the slope is called initial permeability μ_i. As the magnetic field strength is increased there is an irreversible boundary displacement and at first the induced magnetization increases more rapidly and gives a maximum slope μ_{max}. Finally in the upper part of the

magnetization curve all domain boundaries have been displaced and further increase in the magnetic field cause rotation of the domains in the direction of the applied field. At this point the material is saturate, higher fields cannot induce more magnetization. As the magnetic field is decreased to zero, the induced magnetization does not decrease to zero but the alignment of most of the domains during magnetization results in a remanent magnetization or remanence B_r. When the direction of the magnetic field is reversed the induced magnetization decreases and finally becomes zero at a value of the magnetic field strength called the coercive force H_C. Further increased magnetic field strength in this opposite direction eventually causes magnetic saturation in the reverse direction and produces a saturation B_S and remanence B_r values of the same magnitude as in the first quadrant. As an applied field is cycled from one direction to the other direction, the Hysteresis loop is followed. Fig 2.3 shows a typical hysteresis loop of magnetic material. Since the area of the Hysteresis loop represents the energy or work to bring about changes in the magnetic domain structure, the product BH, called the energy product, represents a net loss in the system, usually in the form of heat. A material with a low coercivity is said to be soft and may be used in microwave devices, magnetic shielding, transformers or recording heads. Magnetic materials with high coercivity are called hard and are used to make permanent magnets. Permanent magnets fine application in electric motors and magnetic recording media.
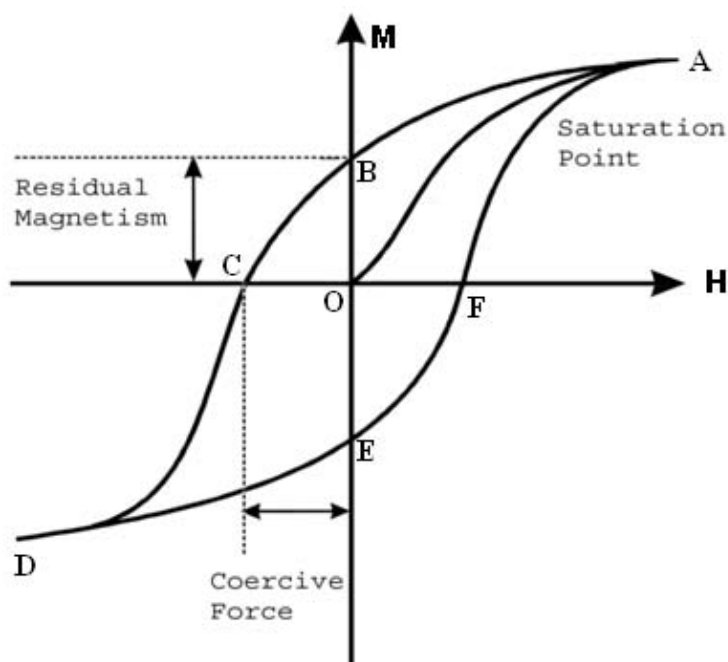
Fig. 2.3 Hysteresis loop of magnetic materials [46].

2.2.4 Maxwell-Wagner polarization

The dielectric constant, ε of a material, is a term that refers to the material's ability to concentrate an electric field. As an example, the higher the dielectric constant of an insulator, the higher the capacitance it can provide when placed between two conducting plates, or in other words, it can store more charge for the same thickness of insulator. The dielectric constant is related to how much a material can be polarized. When placed in an electric field, the atoms, molecules, or ions of a dielectric, respond to the applied electric field (E). It is actually the charges in the dielectric's atoms, molecules, or ions that will reorient themselves in the direction of the applied field. The more responsive are these charges belong to the higher the electric permittivity, ε of the dielectric. Since polarization is the "alignment of permanent or induced atomic or molecular dipole moments with an externally applied electric field [47]. Several sources of polarization exist: space charge, electronics, ionic, and orientation polarization. Typically, dielectric materials exhibit at least one of these polarization mechanisms depending on the material and the manner of the external field frequency as shown in Fig. 2.4.
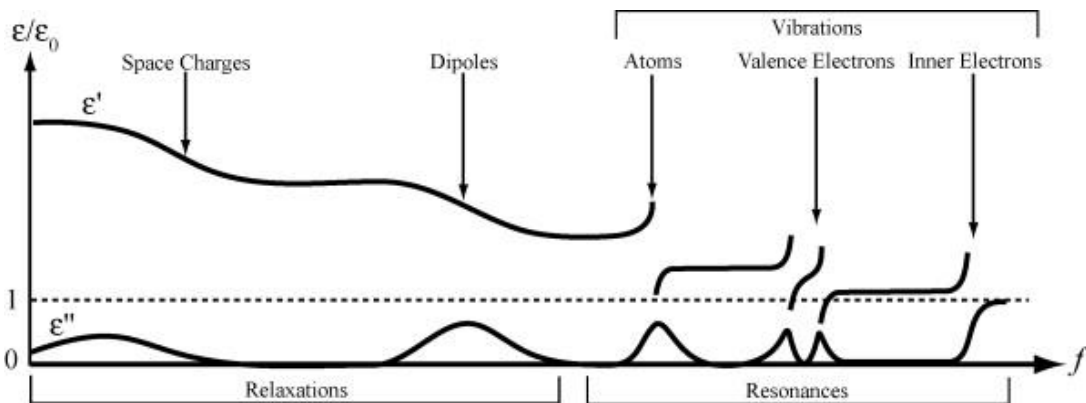
Fig. 2.4 Polarization mechanisms and their effect on the frequency dependence of the relative electric permittivity [48].

The total polarization of a dielectric is consequently equal to the sum of all the polarization mechanisms in the material such as, space charge (P_s), electronic (P_e), ionic (P_{ion}) and orientation (P_o) polarizations.

$$P_{tot} = P_s + P_e + P_{ion} + P_o \tag{2.1}$$

However, the space charges polarization is the so-called Maxwell-Wagner polarization. The electronic, the ionic and the dipole orientation polarization mechanisms have in common that they are caused by the displacement or orientation of bound charge carriers. These carriers are under the influence of the local field which depends on the total applied field and the polarization of the surroundings. However, the space-charge or interfacial polarization mechanism is produced by traveling charge carriers. Thus, the piling up of space-charge in a volume, or of surface charges at an interface, incorporates large-scale field patterns and as such it greatly affects the overall polarizability of a material/structure.

2.2.5 Debye equation of dielectric polarization

To express the dielectric constant in terms of the frequency ω and the relaxation time τ, the definition of the electrical susceptibility equation, $P = (\varepsilon - \varepsilon E)$ gives us for the dielectric constant,

$$\varepsilon(\omega) = 1 + 4\pi\chi(\omega)$$

$$= 1 + 4\pi\chi_e(\omega) + 4\pi\chi_d(\omega) \tag{2.2}$$

Where $\chi_e(\omega)$ and $\chi_d(\omega)$ are the electronic and dipolar susceptibilities respectively. The ionic contribution is very small, and has therefore been ignored. Now in the frequency region in which frequency effects are significant (i.e. the microwave region), $\chi_e(\omega)$ is constant because the electrons are the light particles and thus they can respond to the field instantaneously. Under this condition, $1 + 4\pi\chi_e(\omega)$ is equal to the optical dielectric constant. Finally, recalling from Maxwell's theory that the optical dielectric constant is equal to n^2, where n is the index of refraction, we have from (2.2)

$$\varepsilon(\omega) = n^2 + 4\pi\chi_d(\omega) \tag{2.3}$$

Since χ_d is proportional to α_d by definition, it follows that $\chi_d(\omega)$ has the same complex form as $\alpha_d(\omega)$ and we may then write (2.3) as

$$\varepsilon(\omega) = n^2 + 4\pi\frac{\chi_d(0)}{1 + i\omega\tau} \tag{2.4}$$

$$\varepsilon(\omega) = n^2 + \frac{\varepsilon(0) - n^2}{1 + i\omega\tau} \tag{2.5}$$

Here $\chi_d(0) = \left[\varepsilon^{(0)} - n^2\right]/4\pi$ is the static value of the dipolar susceptibility. This is the equation we set out to seek; it expresses clearly the frequency dependence of the dielectric constant. Now, from the definition of the complex dielectric constant

$$\varepsilon(\omega) = \varepsilon'(\omega) - i\varepsilon''(\omega) \tag{2.6}$$

The following expressions results

$$\varepsilon'(\omega) = n^2 + \frac{\varepsilon(0) - n^2}{1 + i\omega^2 \tau^2} \tag{2.7}$$

$$\varepsilon''(\omega) = \frac{\varepsilon(0) - n^2}{1 + i\omega^2 \tau^2} \omega\tau \tag{2.8}$$

These equation are frequently referred to as the Debye equations [49, 50]. Fig.2.5 shows these equations graphically.
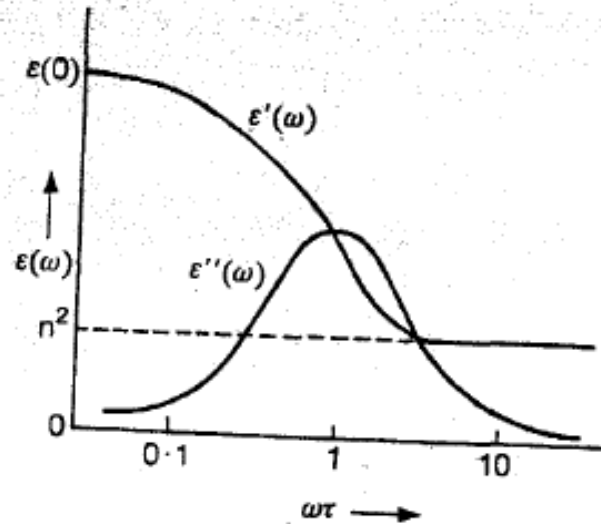
Fig. 2.5 Debye curves for ε' and ε" for a dipolar substance [51].

We note that the real part $\varepsilon'(\omega)$ is a constant, equal to $\varepsilon(0)$ for all frequencies in the range $\omega\tau \ll 1$; this frequency range usually covers all frequencies up to the microwave region. In the frequency range, $\omega\tau \geq 1$, it decreases, eventually reaching the value n^2. This result is quite expected. The imaginary part $\varepsilon''(\omega)$ has its maximum at, $\omega\tau = 1$ and decreases as the frequency departs from this value in either direction.

It may be added here that a part of the electrical energy is dissipated in the dielectric in the form of heat. This is a consequence of the fact that the polarization in alternating fields lags behind in phase relative to the applied field. It can be proved that the rate of this loss is proportional to $\varepsilon''(\omega)$, and is thus maximum at $\omega\tau = 1$.

CHAPTER 3

MATERIALS AND METHOD

3.1 Samples Preparation

3.1.1 Raw materials

Lithium carbonate is the chemical compound with the formula Li_2CO_3. It is notable as being the well-characterized oxide of lithium [52]. There are some physical parameters of Li_2CO_3 as below:

    (i)   Molecular mass is, M = 73.89 g/mol.

    (ii) Density is, ρ = 2.11 g/cc.

    (iii) Melting point is, T_m = 723 °C.

    (iv) Crystal structure is monoclinic.

    (v) Lattice Constant, a = b = 490.7 pm and c = 634.8 pm.

Zinc Oxide is an inorganic compound with the formula ZnO. ZnO is a white powder that is insoluble in water [53]. There are some physical parameters as below:

    (i)   Molecular mass is, M = 81.406 g/mol.

    (ii) Density is, ρ = 5.1 g/cc.

    (iii) Melting point is T_m = 1974 °C and boiling point is T_b = 1974 °C.

    (iv) Crystal structure is Wurtzite

    (v) Lattice Constant, a = 324.95 pm, c = 520.69 pm.

Iron (III) oxide is the inorganic compound with formula Fe_2O_3. It is a red-brown solid [54]. Fe_2O_3 is the main source of iron for the steel industry. There are some physical parameters as following:

    (i)   Molecular mass is, M = 159.687 g/mol.

    (ii) Density is, ρ = 5.25 g/cc.

    (iii) Melting point is, T_m = 1539 °C.

    (iv) Crystal structure is Rhombohedra.

    (v) Lattice Constant, a = 917 pm, b = 930 pm, c = 850 pm.

Vanadium Pentoxide is an inorganic compound with the formula V_2O_5. It is a brown or yellow solid. It is widely used in industrial catalyst [55]. There are few physical parameters as flowing:

(i) Molecular mass is M = 181.88 g/mol.

(ii) Density is, ρ = 3.357 g/cc.

(iii)Melting point is, T_m = 690 ^{o}C and boiling point is, T_b = 1750 ^{o}C.

(iv)Crystal structure is Orthorhombic.

(v) Lattice Constant, a = 1151 pm, b = 355.9 pm, c = 437.1 pm.

3.1.2 Solid state reaction technique

A goal common to all the ferrites is the common formation of the spinel structure. Now a days, Solid State Reaction technique or conventional ceramic process is easier and low cost method. So, major of the ferrite samples are made by the conventional ceramic process or Solid State Reaction technique. The advantages of the mechanical methods include large-scale production of bulk ceramic powder at low cost and comparatively easy adaptability [56]. However, the chemical techniques are generally complex than the conventional solid state reaction and the large-scale production is sometimes difficult. In this research work, the most economical and comparatively simple mixed oxide process (conventional solid-state reaction technique) is used for preparing the different compositions of V_2O_5 added Li-Zn spinel ferrites. In the solid state reaction method, the required composition is usually started form the appropriate amount of raw mineral oxides or carbonates by crushing, grinding and milling. In this research work, the raw mineral oxides are mixed by hand milling in a mortar and pestle and it is in Fig. 3.1. Milling can be carried out to increase the degree of mixing. This method depends on the solid state inter-diffusion between the raw materials. Solids do not usually react at room temperature for normal time scales.

Fig. 3.1 Mortar and Pestle during milling.

Fig. 3.2 A typical programmable electric furnace inside samples.

Thus it is necessary to heat at high temperatures for the diffusion length $(2Dt)^{1/2}$ to except the particle size, where D is the diffusion constant for the fast diffusing species, and t is the firing time. The ground powders can then calcined in air or oxygen at temperature above 800 °C. For some time, this process is continued until the mixture is converted into the correct crystalline phase. The calcined powders are again crushed into the correct crystalline phase. The pellets or toroid shaped samples are prepared from these calcined powders using die-punch assembly or hydrostatic or isostatic pressure. Sintering is carried out in the solid state, at temperature ranging 1000 to 1400 °C, for times of typically 1-40 hours and in various atmospheres (e.g. Air, O_2 and N_2) [57-58]. Fig. 3.3 shows diagrammatically, the stages followed in ferrite preparation. During the calcining stage, the reaction of Fe_2O_3 with metal oxide (say, MeO or Me_2O_3) and adding some Me_2O_3 or Me_2O_5 takes place in the solid state to form spinel according to the reaction:

The general solid state reaction leading to a ferrite $MeFe_2O_4$ may be represented as

$$MeO + Fe_2O_2 \rightarrow MeFe_2O_2$$

Where, Me is the divalent ions.

$$MeO + Fe_2O_3 \longrightarrow MeFe_2O_4 \ (Spinel)$$

$$2Me'_2O_3 + 4Fe_2O_3 \longrightarrow 4Me'Fe_2O_3 \ (Spinel) + O_2$$
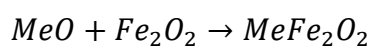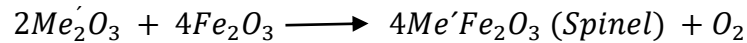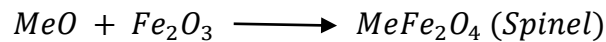
The Li_2CO_3 and ZnO are creeps into Fe_2O_3 as given bellow, to form an intermediate phase

$$Li_2CO_3 + Fe_2O_3 \longrightarrow LiFe_2O_4$$

$$ZnO + Fe_2O_3 \longrightarrow ZnFe_2O_4$$

After the V_2O_5 is added

$$Li_{0.25}O + Zn_{0.50}O + Fe_{2.25}O_3 + xV_2O_5 \longrightarrow Li_{0.25}Zn_{0.50}Fe_{2.25}O_4 + xV_2O_5$$
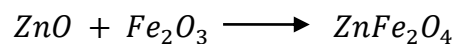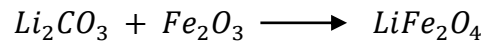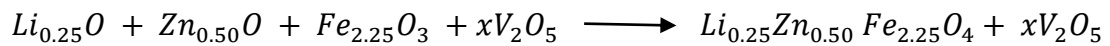
There are basically four steps in the preparation of ferrite:

1. Preparation of materials to form an intimate mixture with the metal ions in the ratio which they will have in the final product.
2. Heating of this mixture to form the ferrite (often called calcining).
3. Grinding the calcined powders and pressing the fine powders into the required shape and
4. Sintering to produce a highly densified product.

The calcining process can be repeated several times to obtain a high degree of homogeneity. The calcined powders are crushed into fine powders. The ideal characteristics of fine powders are [59]:

- Small particle size (sub-micron).
- Narrow distribution in particle size.
- Dispersed particles.
- Equiaxed shape of particle.
- High purity.
- Homogeneous composition.
- A binder is usually added prior to compaction, at a concentration lower than 5 wt%. Binder is polymers or waxes; the most commonly used binder in ferrite is polyvinyl alcohol. During sintering, binders decompose and are eliminated

from the ferrite. Pressures are used for compacting very widely but are commonly several tons per square inch (i.e., up to 10^8 Nm^{-2})

The sintering time, temperature and the furnace atmosphere play very important role on the magnetic property of ferrite materials.

The purposes of sintering process are:

i) To bind the particles tighter so as to impact sufficient to the product,

ii) To density the material by eliminating the pores and

iii) To homogenize the materials by completion the completing the reactions left unfinished in the calcining step.

Sintering of crystalline solids is dealt by Coble and Burke who found the following empirical relationship regarding rate of grain growth:

$$d = kt^a \qquad\qquad (3.1)$$

where d is the mean grain diameter, t is sintering time, a is about 1/3 and k is a temperature dependent parameter.

Sintering is divided into three stages [60].

Stage 1: Contact area between particles increases.

Stage 2: Porosity changes from open to closed porosity.

Stage 3: Pore volume decreases, grains grow

In the initial stage, neighboring particles form a neck by surface diffusion and presumably also at high temperatures by an evaporation-condensation mechanism. Grain growth begins during the intermediate stage of sintering. Since grain boundaries are the sinks for vacancies, grain growth tends to decrease the pore elimination rate due to the increase in distance between pores and grain boundaries, and by decreasing the total grain boundary surface area. In the final stage growth is considerably enhanced and the remaining pores may become isolated.

Block Diagram of sample preparation

| Raw materials (Li_2CO_3, ZnO and Fe_2O_3) |

↓

| Weighing by different weight percentages |

↓

| Hand milling by agate mortar and pestle for 4 h |

↓

| Heating at 750 °C for 3 h in air (calcining) |

↓

| Adding V_2O_5 in different wt% and milling by mortar and pestle for 3 h |

↓

| Adding binder (PVA) and milling in mortar |

↓

| Pressing to desired shape (pellet and toroid) |

↓

| Sintering at temperature (950, 1050 and 1150 °C) for 3h |

↓

| Final products |

Oxides of raw materials.

Weighing by various mole percentage.

Dry mixing for 4 hours by hand milling.

Pressing into disc shapes and calcining at 750 ℃ for 3 hours.

Crushing for 3 hours and adding binder.

Pressing into desired shapes (pellets and toroides) and sintering at 1050 ℃ for 3 hours.

Final Products.

Fig. 3.4 Sample preparation in solid state reaction method.

3.1.3 Preparation of the present samples

The $Li_{0.25}Zn_{0.50}Fe_{2.25}O_4$ + xV_2O_5 (where x = 0.0, 0.4, 0.8, and 1.2wt%) samples were synthesized using the standard solid state reaction technique which discussed in section 3.1.2. Powder of Li_2CO_3, ZnO and Fe_2O_3 were used as raw materials. Stoichiometric amount of required powders were mixed thoroughly and then calcined at 750 °C for 3 hours. The calcined powders were mixed with different proportional V_2O_5 wt% (0.0, 0.4, 0.8, 1.2 wt%). Then, mixed PVA (poly vinyl alcohol) than pressed 15kN pressure into toroid shaped also pressed 20kN and 10kN into pellet shaped samples shown in Fig. 3.5. The samples were sintered at 950, 1050 and 1150 °C temperatures in air for 4 hours. The temperature ramp was 5 °C/minute for both cooling and heating.

(a)   (b)
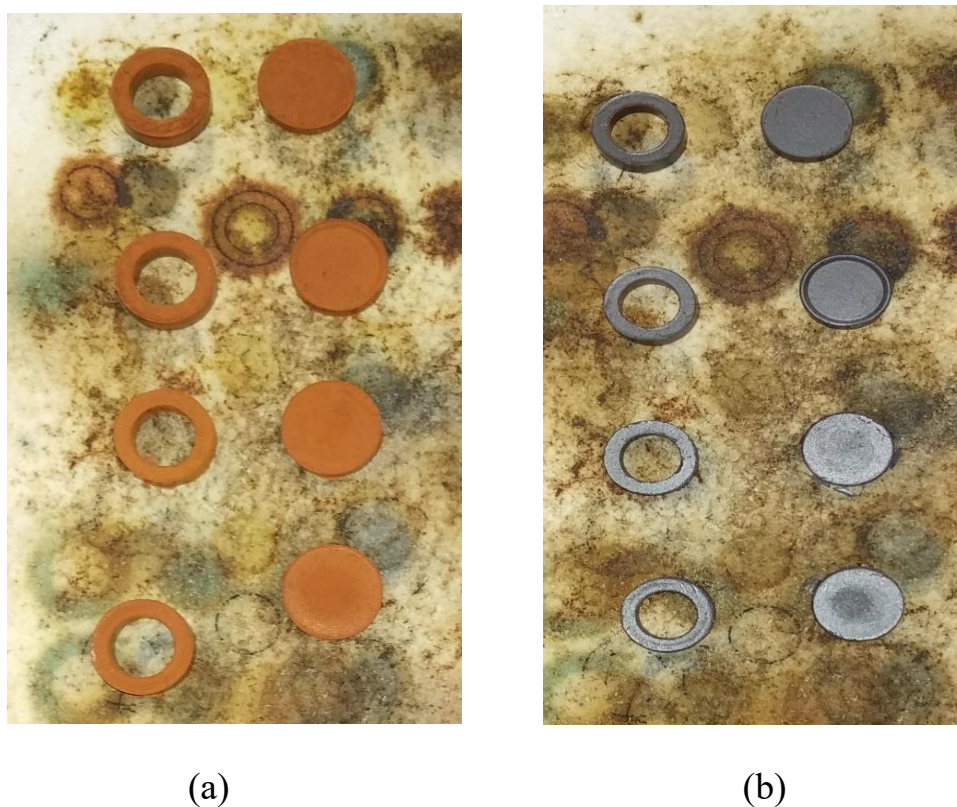
Fig. 3.5 Toroid and cylindrical shaped samples put on ceramics plate (a) before sintering (b) after sintering.

3.2 Characterization

3.2.1 The X-ray diffraction

The X-ray diffraction provides precise knowledge of the lattice parameter as well as the substantial information on the crystal structure of the material under study. XRD is one of the most effective tools for the determination of phase in a sample. X-rays are the electromagnetic waves whose wavelengths are in the neighborhood of 1 Å. The wavelength of an X-ray is thus of the same order of magnitude as the lattice constant of crystals. Whenever X-rays are incident on a crystal surface, they are reflected from it. This is called Bragg reflection. Fig. 3.6 shows the phenomenon of Bragg reflection. If a beam of monochromatic radiation of wavelength λ incident on a periodic crystal plane at an angle θ and is diffracted in the same angle, this event abides by the celebrated Bragg's law which is given below

$$2dsin\theta = n\lambda \tag{3.2}$$

Here d is the distance between crystal planes, and n is positive integer. Bragg's law also suggests that the diffraction is only possible when λ <2d [61].
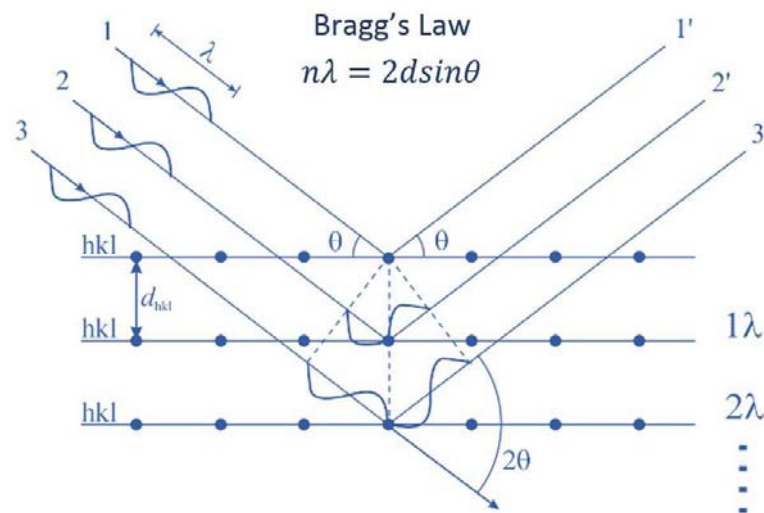
Fig. 3.6 Geometry of the incident X-rays impinging the sample satisfying Bragg's law [45].

XRD is a versatile non-destructive analytical technique for identification and quantitative determination of various crystalline phases of powder or solid samples of

any compound. A Rigaku Smartlab X-ray diffraction system was used to get X-ray data for the samples at the Materials Science Division, Atomic Energy Center, Dhaka, which is a sophisticated X-ray diffractometer installed very recently. The powder diffraction technique was used with a primary beam power of 40 kV and 30mA for Cu radiation. A nickel filter was used to reduce Cu-K$_a$ radiation and finally Cu-K$_a$ radiation was only used as the primary beam. A $(\theta - 2\theta)$ scan was taken from 15° to 75° to get possible fundamental peaks of the sample with the sampling pitch of 0.02° and time for each step data collection was 1.0 sec. Both the programmable divergence and receiving slits were used to control the irradiated beam area and output intensity from the sample respectively.

3.2.2 Interpretation of the XRD data

The XRD data consisting of θ_{hkl} and d_{hkl} values corresponding to the different crystallographic planes are used to determine the structural information of the samples like lattice parameter and constituent phase.

The lattice parameter for each peak of each sample was calculated by using the formula:

$$a = d_{hkl} \times \sqrt{a^2 + b^2 + c^2} \qquad (3.3)$$

Where, h, k and l are the indices of the crystal planes. To determine the exact lattice parameter for each sample, Nelson-Riley method was used. The Nelson-Riley function F(θ), can be written as

$$F(\theta) = \frac{1}{2}\left(\frac{cos^2\theta}{Sin\theta} + \frac{cos^2\theta}{\theta}\right) \qquad (3.4)$$

Now drawing the graph of 'a' vs F(θ) and using linear fitting of those points will give us the lattice parameter 'a'. This is the value of 'a' at F(θ) =0.

3.2.3 X- Ray density and bulk density determination

X-ray density ρ_x was also calculated using the lattice parameter. The relation between ρ_x and a is as follows:

$$\rho_x = \frac{8M}{Na^3} \, gcm^{-3} \qquad (3.5)$$

where N is the Avogadro's number (6.02×10^{23} mol^{-1}), M is the molecular weight. The bulk density, ρ_B is measured by the formula [62],

$$\rho = \frac{M}{V} \tag{3.6}$$

Where, M is the mass of the disc sample and V its volume. Porosity (P%) in percentage was calculated using the

$$P = \left(1 - \frac{\rho_B}{\rho_x}\right) \times 100 \tag{3.7}$$

3.2.4 The study of field emission scanning electron microstructure

Sensitivity of electrical and magnetic properties depends on the microstructure of the ferrite sample. Permeability is directly proportional to grain size, At least up to a critical diameter of the grains permeability increases monotonically. Density and resistivity depends on the porosity of the sample. So study of microstructure is necessary for making prediction about the result of permeability and resistivity. Fig. 3.7 shows the experimental setup for FESEM. The SEM microstructure of samples sintered at 1050 ºC was studied by Scanning Electron Microscope. To observe the microstructure, the ferrite samples were polished with fine Al_2O_3 powder followed by thermal etching from 800-900 ºC for all samples. When the etching was completed, the grains were seen clearly by the SEM. The average grain size was calculated by the linear intercept method.

Fig. 3.7 Field Emission Scanning Electron Microscope setup.

3.2.5 Saturation magnetization measurement

Magnetization is defined as the magnetic moment per unit volume. There are various techniques of measuring magnetization of a substance. Vibrating sample magnetometer, as the name implies, vibrate the sample as part of the measurement process. This provides the flux meter element of the system with the dynamic component which it requires to make the measurement. The applied field is changed so, at each measurement point the field is static and hence no eddy currents to cause problems. The objective when using a VSM or any other type of magnetic characterization system is to obtain the dependence of the magnetization on the applied field. Fig. 3.8 shows the experimental setup for M-H measurement.

Fig. 3.8 The DYNACOOL physical property measurement system.

The sample, usually a sphere or small disc, is cemented to the lower end of a rod, the other end of which is fixed to a mechanical vibrator. Current through the vibrator and vibrate the rod at about 37 Hz with amplitude of about 7 V in a direction at right angles to the magnetic field. The oscillating magnetic field of the sample induces an alternation emf in the direction coils. The vibrating rod also carries a reference specimen, in the form of a small permanent magnet near its upper end; the oscillating field of this induces another emf in two reference coils. The two voltage form two sets of coils are compared, and the difference is proportional to the magnetic moment of the sample. The

magnetization measurement was performed ranged from -2 T to +2 T magnetic field for all samples.

3.2.6 Complex permeability measurement

For high frequency application, the desirable properly of a ferrite is the high permeability with low loss. The present goal of most of the recent ferrite researchers is to fulfill this requirement. Permeability is namely defined as the proportional constant between the magnetic field induction B and applied field intensity H [63]:

$$B = \mu H \tag{3.8}$$

If a magnetic material is subjected to an AC magnetic field as given below;

$$H = H_0 e^{i\omega t} \tag{3.9}$$

Then, it is observed that the magnetic flux density B experiences a delay. This delay is caused due to presence of various losses and is thus expressed as

$$B = B_0 e^{i(\omega t - \delta)} \tag{3.10}$$

where δ is the phase angle and marks the delay of B with respect to H. The permeability is then given by

$$\mu = \frac{B}{H} = \frac{B_0 e^{i(\omega t - \delta)}}{H_0 e^{i\omega t}} = \frac{B_0 e^{-i\delta}}{H_0} = \mu' - i\mu'' \tag{3.11}$$

$$\text{where} \quad \mu' = \frac{B_0}{H_0} \cos\delta \, , \mu'' = \frac{B_0}{H_0} \sin\delta \tag{3.12}$$

The real part μ' of complex permeability μ as expressed in equation (3.11) represents the component of B which is in phase with H, so it corresponds to the normal permeability. If there are no losses, we should have $\mu = \mu'$. The imaginary part μ'' corresponds to that part of B which is delayed by phase angle ranging up to 90° from H. The presence of such a component requires a supply of energy to maintain the alternating magnetization, regardless of the origin of delay. The ratio of μ'' to μ', as is evident from equation (3.12) gives

$$\frac{\mu''}{\mu'} = \frac{\frac{B_0}{H_0} \sin\delta}{\frac{B_0}{H_0} \cos\delta} = \tan\delta \tag{3.13}$$

This $tan\,\delta$ is called the Loss Factor or Loss tangent. The Q-factor or quality factor is defined as the reciprocal of this loss factor, i.e.

$$Q = \frac{1}{tan\delta} \tag{3.14}$$

Measurements of permeability normally involve the measurements of the change in self- inductance of a coil in presence of the magnetic core. The behavior of a self-inductance can now be described as follows. Suppose we have an ideal lossless air coil of inductance, L_o. On insertion of magnetic core with permeability μ, the inductance will be μL_0. The complex impedance Z of this coil can be expressed as

$$Z = R + jX = j\omega L_0\mu = j\omega L_0(\mu' - j\mu'') \tag{3.15}$$

where the resistive part is

$$R = \omega L_0\mu' \tag{3.16}$$

and the reactive part is

$$X = \omega L_0\mu' \tag{3.17}$$

The radio frequency (RF) permeability can be derived from the complex impedance of a coil Z. The frequency characteristics of the Li-Zn ferrite + xV_2O_5 wt% samples i.e. the permeability spectra were investigated using Wayne Kerr Impedance Analyzer (6500B). The measurements of inductances were taken in the frequency range of 20Hz to 120MHz. Fig. 3.9 shows the experimental setup for permeability measurement.
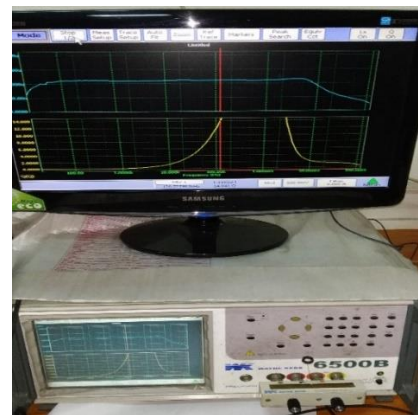
(a)   (b)

Fig. 3.9 Wayne Kerr Impedance Analyzer (6500B) (a) experimental setup (b) during permeability measurements.

Fig. 3.10 Toroid shaped sample for the measurement of permeability.

The real and the imaginary part of permeability are calculated. μ' is calculated by using the following formula:

$$L_s = L_0\mu' \qquad (3.18)$$

And,

$$\tan\delta = \frac{\mu''}{\mu'} \qquad (3.19)$$

where $\tan\delta$ is loss factor and L_s is the self-inductance of the sample core given as

$$L_s = \frac{\mu_0 N^2 S}{\pi\bar{d}} \qquad (3.20)$$

where L_0 is the inductance of the winding coil without the sample core and N is the number of turns of coil (here N = 5), S is the area of cross section of the toroid as given below

$$s = dh; \text{h} = \text{height} \qquad (3.21)$$

where

$$d = \frac{(d1 \sim d2)}{2}, \qquad (3.22)$$

$$\bar{d} = \frac{d_1 + d_2}{2} \qquad (3.23)$$

By applying a comparatively small sinusoidal signal of amplitude A and frequency f to the capacitor, the displacement current I through the capacitor and the voltage V across the capacitor can be measurement by using an Impedance Analyzer and find the complex impedance Z from the Ohm's Law.

$$\frac{V}{I} = Z = R - jX = Z \tag{3.24}$$

$$X = \frac{1}{2\pi f C} \tag{3.25}$$

When the capacitor under test is small, the reactance X will be large and possibly affected by a parasitic resistance. On the other hand, if the capacitance under test is typically larger than the reactance will be small and likely to be affected by a series resistance.

The value of the dielectric constant ε' can easily be evaluated by using the parallel plate capacitor equation when the capacitance is found

$$\varepsilon' = \frac{Cd}{\varepsilon_o A} \tag{3.26}$$

where C is the capacitance of the dielectric measurement in "F", d is the thickness of the shaped sample measurement in "m", ε_o is the permittivity of the free space (8.854×10^{-12} Fm^{-1}) and A is the cross sectional area of the electrode measured in "m^2".

3.2.7 Electrical resistivity measurement

Electrical resistivity of the samples has been measured by two probe method. Samples were prepared by sintering temperature of 1050 °C. The samples were polished with the help of emery paper with grit size 800 and 1000 successively. Then silver paste was added to the both sides of the polished samples together with two thin copper wires of 100 micron diameter. The resistivity has been calculated using the formula

$$\rho = \frac{RA}{l} \tag{3.27}$$

where ρ is the resistivity, l and A are the thickness and the area of the sample, respectively.

3.2.8 Dielectric constant measurement

A dielectric material is typically an insulator which is polarized when subjected to an applied electric field. Basically the study of dielectric properties involves the storage and dissipation of electric and magnetic energy in materials. Typically the measurement of dielectric constant involves the measurement of capacitance C_0 of a test capacitor with vacuum between its plates. Then using the same capacitor and maintaining the same distance between its plates, the capacitance C with a dielectric material between the plates is measured. The simplest capacitor structure is a pair of parallel conducting plates separated by a medium called the dielectric. The value of the capacitance between the plates is given by the equation.

$$C_0 = \frac{\varepsilon A}{d} \tag{3.28}$$

where A is the area of the plates, d is the separation between the plates and ε is the absolute permittivity of the dielectric, which is a measure of the electrostatic energy stored within it and therefore dependent of the material. The dielectric constant of the medium (also known as the relative permittivity) is defined as

$$\varepsilon_r = \frac{\varepsilon}{\varepsilon_0} \tag{3.29}$$

where ε_0 is the permittivity of free space, which has value of 8.85×10^{-12} Fm^{-1}.

3.2.9 Impedance spectroscopy

For investigating the electrical properties of materials the complex spectroscopy is a very powerful tool. Typically a Wheatstone-bridge type setup (LCR meter or Impedance Analyzer) is used for ac measurements. In this technique, the resistance R and capacitance C of the specimen are measured and balanced against variable resistors and capacitors. The technique in which the impedance $|Z|$ and the phase difference (θ) between the voltage and current are measured as a function of frequency for the given specimen in known as impedance spectroscopy. For the analysis of obtained data a plot (a plot between the imaginary part of the impedance $Z'' = |Z|cos\theta$ and the real part $Z' = |Z|sin\theta$ on a complex plane) is dawn. Generally an impedance plot with linear scale is used for analyzing the equivalent circuit. Impedance plot of a pure capacitor is a

straight line coincides with the imaginary axis and that of pure resistor defines a point on the real axis. The following relation is used to express the impedance of a parallel RC combination [64]

$$Z^* = Z' - jZ'' \qquad (3.30)$$

$$Z^* = \frac{R}{(1 + j\omega RC)} \qquad (3.31)$$

After simplification, we get

$$\left(Z' - \frac{R}{2}\right)^2 + (Z'')^2 = \left(\frac{R}{2}\right)^2 \qquad (3.32)$$

This equation represents a circle of radius $\frac{R}{2}$ and centre at $(\frac{R}{2}, 0)$. Therefore, a plot between Z′ and Z′′ will represent a semicircle of radius $\frac{R}{2}$ as shown in Fig. 3.11 (a). This plot is often known as Nyquist plot. The time constant of a simple circuit can be written as,

$$\tau = Rc = \frac{1}{\omega_0} \qquad (3.33)$$

This relation to the relaxation time of the specimen and the characteristic frequency lies at the peak of the semi-circle. At high frequency, the impedance plot exhibits an arc related to the bulk property of an ideal specimen. Whereas an arc at low frequency corresponds to the grain boundary behavior and a spike at the lowest frequency is related to the electrode effect. A typical impedance plot and the equivalent circuit for a polycrystalline material are illustrated in Fig. 3.11 (b). In this thesis, a precision Impedance Analyzer (Wayne Kerr Impedance Analyzer, 6500B) is used for the measurement of real (Z′) and imaginary (Z′′) part of the complex impedance as a function of frequency at room temperature.
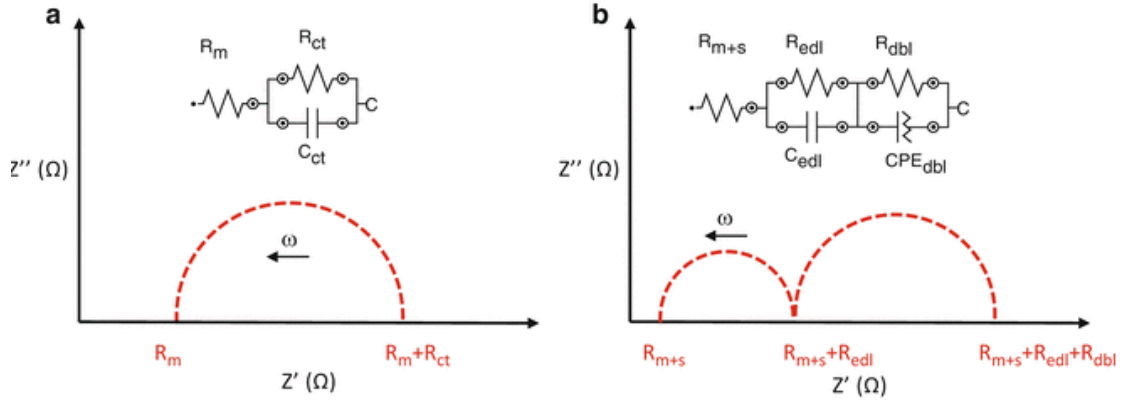
Fig. 3.11 (a) An impedance plot with the corresponding equivalent circuit and (b) Impedance plot an ideal polycrystalline sample with the equivalent circuit.

3.2.10 Complex modulus analysis

Complex modulus is a convenient and important tool for analyzing, interpreting and calculating conductivity relaxation times, ion or charge carrier hopping rate, etc. It also provides an alternative approach to analyze the electrical response of the materials. It was measured by the equation (3.34),

Complex Modulus (M^*),

$$M^*(\omega) = M' + jM'' = \frac{1}{\varepsilon^*}$$

$$= j\omega C_0 Z^* \tag{3.34}$$

where the real part of the modulus is $M' = \omega C_0 Z''$, imaginary part is $M'' = \omega C_0 Z'$ (ω denotes the angular frequency) and C_0 is the capacitance discussed earlier. We know that the electrical complex modulus can easily differentiate the localized (i.e., dielectric relaxation) and delocalized (i.e., long-range) conduction. The space charge relaxation mechanism can also be explained easily by the study of modulus. [65].

CHAPTER 4

RESULTS AND DISCUSSION

4.1 Introduction

The influence of V_2O_5 addition on the structural, microstructural, electrical and magnetic properties of Li-Zn ferrites having the compositions $Li_{0.25}Zn_{0.50}Fe_{2.25}O_4$ + xV_2O_5 (where x = 0.0, 0.4, 0.8 and 1.2 wt %) are reported in the present study. The samples were sintered at different temperatures. Various experimental studies such as structural characterization, microstructural feature, magnetic hysteresis loop, complex permeability spectra, dielectric constant, dielectric loss factor, ac electrical conductivity and impedance spectroscopy of V_2O_5 added Li-Zn ferrites are discussed in this chapter.

4.2 Structural Property

4.2.1 X-ray diffraction

In order to study of the crystal structure of V_2O_5 (0.0, 0.4, 0.8 and 1.2 wt%) added Li-Zn ferrites, an XRD technique were performed for all the prepared samples sintered at 1050 ºC with Cu-K_α radiation (λ = 0.15405 nm).

Fig. 4.1 XRD pattern of $Li_{0.25}Zn_{0.50}Fe_{2.25}O_4$ + xV_2O_5 sintered at 1050 °C.

Fig. 4.2 Variation of the apparent lattice parameter, a (Å) with $F(\theta)$ for the various compositions $Li_{0.25}Zn_{0.50}Fe_{2.25}O_4 + xV_2O_5$ sintered at 1050 ^{o}C.

The XRD pattern of V_2O_5 (0.0, 0.4, 0.8 and 1.2 wt%) added Li-Zn ferrites is shown in Fig. 4.1. It is observed that the crystalline structure of all the samples has been confirmed the cubic spinel structure with the manifestation of (111), (220), (311), (222), (400), (422), (511) and (440) fundamental reflection planes [66]. The prepared samples are in single phase without any other detectable secondary phase. It is also found that there has not been observed structural transition in the synthesized samples. The strongest reflection peak is observed for all the samples at (311) plane, which signifies the spinel phase. The XRD pattern of V_2O_5 (0.0, 0.4, 0.8 and 1.2 wt%) added Li-Zn ferrites was compared with JCPDS (Joint Committee on Powder Diffraction Standards) data and it matches very well with file (JCPDS card no. 37-1471).The lattice parameter was calculated from the XRD data using Nelson-Riley (N-R) function, $F(\theta)$ [67]. The variations of apparent lattice parameter (a) with $F(\theta)$ are given in Fig. 4.2 for different compositions. The intersection on Y-axis at $F(\theta) = 0$ gives the desired lattice constant. This is shown in Table 4.1. The tetrahedral (A) site radii (r_A) , octahedral (B) site radii (r_B), tetrahedral bond length (d_{AX}), octahedral bond length (d_{BX}) were

calculated with the help of lattice constant, oxygen positional parameter (u = 0.381 Å) and oxygen ion radius (R_o = 1.32 Å) from the following relations [22]. These are tabulated in Table 4.1. There is a good correlation between the lattice constant and the ionic radii of the octahedral sites. It clearly indicates that the lattice constant remains constant due to addition of V_2O_5 content, which could be attributed to the unchanged of the ionic radii of the octahedral sites. Therefore, it is assumed that V_2O_5 has not been influenced on the phase formation of Li-Zn ferrites. This result demonstrated that there is no reaction occurred between V_2O_5 and Li-Zn ferrites throughout the sintering process [28].

$$r_A = (u - 0.25)a\sqrt{3} - R_0 \tag{4.1}$$

$$r_B = (0.625 - u)a - R_0 \tag{4.2}$$

$$d_{AX} = a\sqrt{3}(u - \tfrac{1}{4}) \tag{4.3}$$

$$d_{BX} = a\sqrt{[3u^2 - \left(\tfrac{11}{4}\right)u + (\tfrac{43}{64})]} \tag{4.4}$$

The hopping length in the tetrahedral (L_A) site and octahedral (L_B) site can also be evaluated from the following relations [68-69]. These are shown in Table 4.1.

$$L_A = \frac{a\sqrt{3}}{4} \tag{4.5}$$

$$L_B = \frac{a\sqrt{2}}{4} \tag{4.6}$$

Table 4.1 Lattice constant (a), tetrahedral (A) site radius (r_A), octahedral (B) site radius (r_B), tetrahedral bond length (d_{AX}), octahedral bond length (d_{BX}), hopping length of tetrahedral site (L_A) and octahedral site (L_B) for $Li_{0.25}Zn_{0.5}Fe_{2.25}O_4$ + xV_2O_5 sintered at 1050 °C.

V_2O_5 content (wt%)	a (Å)	r_A (Å)	r_B (Å)	d_{AX} (Å)	d_{BX} (Å)	L_A (Å)	L_B (Å)
0.0	8.394	0.585	0.728	1.905	2.049	3.635	2.968
0.4	8.389	0.583	0.727	1.903	2.048	3.633	2.966
0.8	8.391	0.584	0.727	1.904	2.049	3.633	2.967
1.2	8.401	0.586	0.730	1.906	2.051	3.638	2.970

4.2.2 X-ray density, bulk density and porosity

Fig. 4.3 Variation of ρ_B with different V_2O_5 contents of $Li_{0.25}Zn_{0.50}Fe_{2.25}O_4$ for T_s.

Fig. 4.3 depicts the variation of bulk density (ρ_B) of $Li_{0.25}Zn_{0.50}Fe_{2.25}O_4$ with different amount of V_2O_5 addition for various sintering temperatures (T_s = 950, 1050 and 1150 ℃) in air for 3 h. It clearly demonstrates that the densification of the prepared samples is larger for T_s = 1050 ℃ in compared to 950 and 1150 ℃ sintering temperatures. It clearly indicates that the optimum sintering is to be about 1050 ℃ for the present samples, which is considered for further investigation. ρ_B, ρ_x and P of the studied samples were calculated and tabulated in Table 4.2. It is found that ρ_B increases with the increase of V_2O_5 content (upto 0.8 wt% V_2O_5) and then decreased for 1.2 wt% V_2O_5. It demonstrates that ρ_x is higher than that of ρ_B which may be attributed to the existence of pores [70]. The variation of P with V_2O_5 content is shown in Table 4.2. It is observed that the P decreases with the addition of V_2O_5, which could be ascribed to the enhancement of densification of sintered samples [30]. The porosity of the samples decreased with the addition V_2O_5 contents, which could be attributed to the role of V_2O_5 as sintering aid to enhance the densification of the ferrite samples from 4.30 g/cm^3 (for x = 0.0 wt% V_2O_5) to 4.51 g/cm^3 (for x = 0.8 wt% V_2O_5). However, the porosity

slightly increased for x = 1.2 wt% V_2O_5. For the content higher than 0.8 wt%, the decrease of density might be attributed to the reduction of diffusion rate due to an increase in the liquid layer thickness [25].

Table 4.2 X-ray density, bulk density and porosity of $Li_{0.25}Zn_{0.50}Fe_{2.25}O_4$ with various V_2O_5 contents sintered at 1050 °C.

Compositions	ρ_x (g/cm^3)	ρ_B (g/cm^3)	P (%)
$Li_{0.25}Zn_{0.50}Fe_{2.25}O_4$	5.04	4.30	15
$Li_{0.25}Zn_{0.50}Fe_{2.25}O_4$ + 0.4 V_2O_5 wt%	5.04	4.37	13
$Li_{0.25}Zn_{0.50}Fe_{2.25}O_4$ + 0.8 V_2O_5 wt%	5.02	4.51	10
$Li_{0.25}Zn_{0.50}Fe_{2.25}O_4$ + 1.2 V_2O_5 wt%	5.03	4.42	12

4.3 Surface Morphology

4.3.1 Microstructural analysis

The FESEM images of the Li-Zn ferrites sintered at 1050 °C with various V_2O_5 (0.0, 0.4, 0.8 and 1.2 wt%) contents are shown in Fig.4.4. These photomicrographs were performed at the same magnification for all the samples. It clearly shows that the grain growth of Li-Zn ferrites strongly depends on the V_2O_5 addition. Histograms of grain sizes with corresponding V_2O_5 contents are shown in Fig.4.5. The average grain sizes (*D*) are obtained with the help of Gaussian fitting and is tabulated in Table 4.3. In Fig.4.5 (a-c), the average grain size of the samples increases from 5.3 μm for x = 0.0 wt% V_2O_5 to 7.7 μm for x = 0.8 wt % V_2O_5. The increase of grain size could be attributed to the promote grain growth and densification of the samples [71-73]. However, the grain size is reduced as shown in Fig. 4.3 (d) which was found to be 6.6 μm for x = 1.2 wt % V_2O_5. This is because the higher excess amount of V_2O_5 is reduced the diffusion rate due to an increase of the liquid layer thickness resulting in decrease of grain growth. Moreover, the presence of liquid phase during sintering allows particle

rotation and grain annexation effect resulting in forming abnormal crystal grains and deteriorating the homogeneity [74-76].
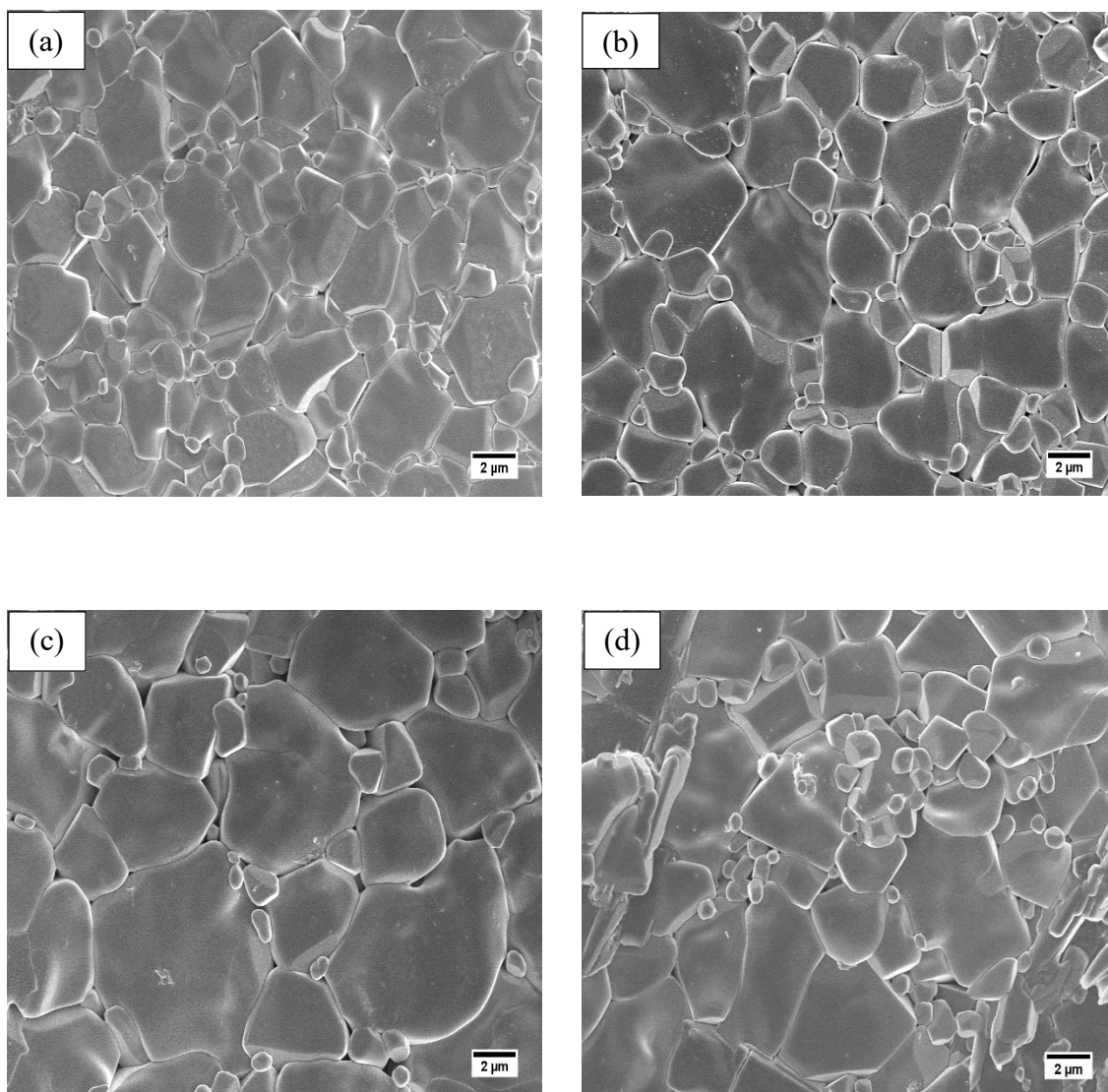
Fig. 4.4 FESEM images of $Li_{0.25}Zn_{0.50}Fe_{2.25}O_4$ sintered at 1050 °C with different V_2O_5 additions (a) 0.0 wt%, (b) 0.4 wt%, (c) 0.8 wt% and (d) 1.2 wt%.

Table 4.3 Data for average grain size of $Li_{0.25}Zn_{0.50}Fe_{2.25}O_4 + xV_2O_5$ sintered at 1050 °C.

Compositions	D (μm)
$Li_{0.25}Zn_{0.50}Fe_{2.25}O_4 + 0.0$ wt% V_2O_5	5.3
$Li_{0.25}Zn_{0.50}Fe_{2.25}O_4 + 0.4$ wt% V_2O_5	5.9
$Li_{0.25}Zn_{0.50}Fe_{2.25}O_4 + 0.8$ wt% V_2O_5	7.7
$Li_{0.25}Zn_{0.50}Fe_{2.25}O_4 + 1.2$ wt% V_2O_5	6.6

Therefore, the microstructural characteristic demonstrates that the grain growth of Li-Zn ferrites is highly affected by V_2O_5 additive contents that may influence the magnetic properties.

Fig. 4.5 Histogram of grain size distribution for different composition of Li-Zn ferrites.

4.3.2 Energy dispersive spectroscopy analysis

(a)

(b)

(c)

(d)
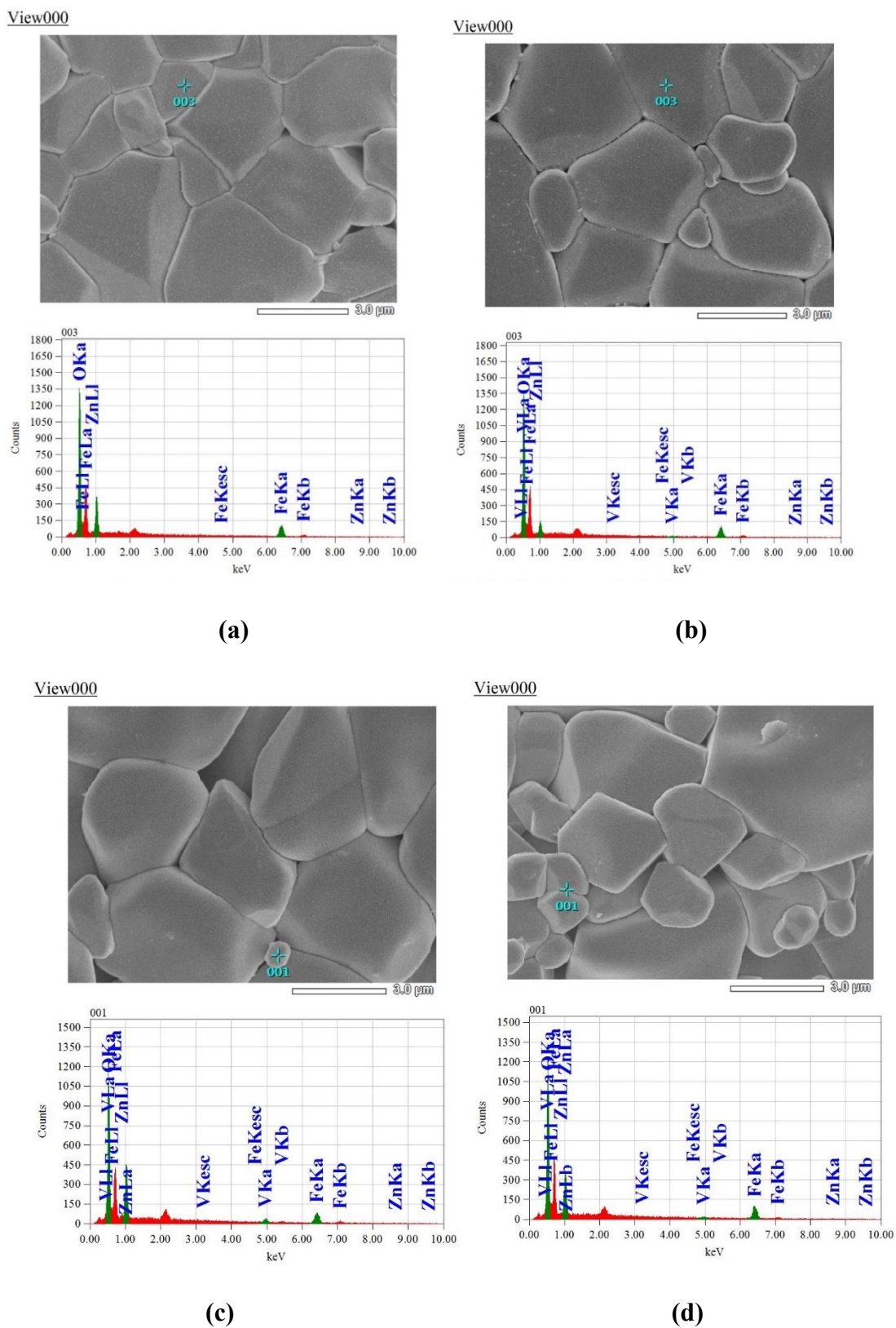
Fig. 4.6 EDX Spectra of $Li_{0.25}Zn_{0.50}Fe_{2.25}O_4 + xV_2O_5$, where (a) x = 0.0 wt%, (b) x = 0.4 wt%, (c) x = 0.8 wt% and (d) x = 1.2 wt% sintered at 1050 $^{\circ}$C.

The quantitive elemental analysis EDS spectra of $Li_{0.25}Zn_{0.50}Fe_{2.25}O_4 + xV_2O_5$ samples (where x = 0.0, 0.4, 0.8 and 1.2 wt %) are shown in Fig. 4.6. It is clearly found that the ferrites are made up of the respective elements, as no extra peak has appeared in the EDS spectra. Therefore, the solid state reaction method in this reaserch work is an appropriate for performing good stoichiometry in the spinel ferrite. Data of elemental analysis for studing compositions of $Li_{0.25}Zn_{0.50}Fe_{2.25}O_4 + xV_2O_5$ is given in Table 4.4. It is observed that the bulk material are fully stoichiometric.The presence of O, V, Fe and Zn are ensured in the spinel ferrites samples. It is also observed that the Li is not present in all the samples because of lower energy of characteristic radiation.

Table 4.4 Data of EDX for $Li_{0.25}Zn_{0.50}Fe_{2.25}O_4 + xV_2O_5$ spinel ferrites.

Sample	Elements	Mass %	Atom %
$Li_{0.25}Zn_{0.50}Fe_{2.25}O_4$	O	31.39	62.01
	V	0.00	0.00
	Fe	58.42	33.06
	Zn	10.20	4.93
	Total	100.00	100.00
$Li_{0.25}Zn_{0.50}Fe_{2.25}O_4 + 0.4$ wt% V_2O_5	O	37.02	67.55
	V	0.90	0.52
	Fe	55.31	28.91
	Zn	6.77	3.03
	Total	100.00	100.00
$Li_{0.25}Zn_{0.50}Fe_{2.25}O_4 + 0.8$ wt% V_2O_5	O	32.83	63.95
	V	4.36	2.67
	Fe	42.26	23.58
	Zn	20.55	9.80
	Total	100.00	100.00
$Li_{0.25}Zn_{0.50}Fe_{2.25}O_4 + 1.2$ wt% V_2O_5	O	31.73	62.70
	V	1.06	0.66
	Fe	50.28	28.46
	Zn	16.93	8.18
	Total	100.00	100.00

4.4 Magnetic Property

4.4.1 Magnetic hysteresis loop: M-H curve

The magnetic hysteresis curves and their properties such as the saturation magnetization (M_s) and coercivity (H_c) are very useful information from the application point of view. Fig. 4.7 shows the variation of the magnetization (M) with the applied magnetic field strength (H) at room temperature for $Li_{0.25}Zn_{0.50}Fe_{2.25}O_4 + xV_2O_5$ compositions (where x = 0.0, 0.4, 0.8 and 1.2 wt%) for the sintering temperature of 1050 °C at constant frequency, f = 40 Hz. The M-H hysteresis curve was performed in the range of applied field upto ~2 T. The magnetization increases sharply with increasing of applied magnetic field for all the samples. After that the magnetization increase slowly and it becomes saturated. It clearly demonstrates that all the samples have shown the hysteresis behavior with applied magnetic field strength. It also indicates the value of saturation magnetization is larger for x = 0.8 wt% V_2O_5 in compared to the other compositions. This could be attributed to the enhancement of grain size or densification.
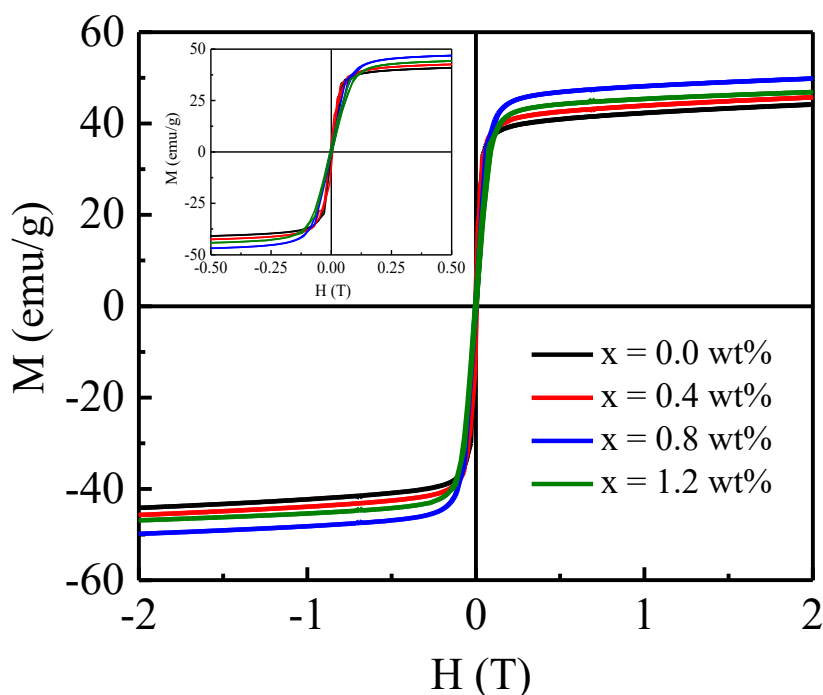
Fig. 4.7 Magnetic hysteresis curve (*M-H*) for different compositions of $Li_{0.25}Zn_{0.50}Fe_{2.25}O_4 + xV_2O_5$ at 300K.

4.4.2 Saturation magnetization, coercivity and experimental magnetic moment

The magnetic moment of the spinel ferrite depends on the cation distributions between tetrahedral (A-site) and octahedral (B-site) in the spinel sub-lattices. According to Neel's theorem of ferrimagnetism, $J_{AB} \gg J_{BB} \gg J_{AA}$ [77], where J_{AB} indicates the A-B super-exchange interaction, J_{BB} and J_{AA} are represented the exchange interactions of A-A and B-B, respectively.

The cation distribution of $Li_{0.25}Zn_{0.50}Fe_{2.25}O_4$ can be written as

$$(Zn_{0.50}^{2+}Fe_{0.50}^{3+})_A \ [Li_{0.25}^{+}Fe_{1.75}^{3+}]_B O_4^{2-}$$
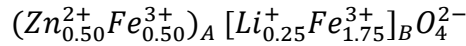
where the first bracket represents A-sites and the square bracket represents B-sites. Blasse has shown that V^{5+} ions have preferred to A-sites due to its stable electrostatic interaction in the spinel lattice [78]. However, the probability of V^{5+} ions occupying in B-sites cannot be overlooked. The value of M_S of $Li_{0.25}Zn_{0.50}Fe_{2.25}O_4$ is relatively lowered (for 0.0 wt% V_2O_5) in compared to other samples, which may be related to smaller grains and lower density of the materials. But the value of M_S increases with the amount V_2O_5 addition which could be attributed to the enhancement of densification of the samples and prompt grain growth [26]. This result is consistent with the microstructural change. The magnetic hysteresis analysis demonstrated that the M_S was increased from 44.0 (for x = 0.0 wt%) to 50.3 emu/g (for x = 0.8 wt% V_2O_5). However, the M_S was found to decrease for x = 1.2 wt% V_2O_5, which may be related to weaken of exchange interaction due to the introduction of excess non-magnetic V_2O_5 [30]. Thus, the M_S is reduced at higher content of V_2O_5. The experimental magnetic moment (n_{exp}) was calculated from the following relation [79, 80]

$$n_{exp} = \frac{(M_W \times M_S)}{5585} \tag{4.7}$$

where M_W is the molecular weight of the sample. The values of n_{exp} are presented in Table 4.5. It is observed that n_{exp} increases with the addition of V_2O_5 additives (upto 0.8 wt%). However, the value of n_{exp} is found to decrease for 1.2 wt%. This may be ascribed to the existence of an excess liquid phase which gives rise to the formation of pores resulting in the hinder of the magnetization process due to excess non-magnetic V_2O_5. Coercivity (H_c) for all the samples are found and given in Table 4.5. It is observed

that the values of coercivity are smaller ($H_c < 75\ Oe$), which reveals the magnetic softness nature of the materials [81].

Table 4.5 Data for saturation magnetization, coercivity and experimental magnetic moment.

Compositions	M_s (emu/g)	H_c (Oe)	n_{exp} (μ_B)
$Li_{0.25}Zn_{0.50}Fe_{2.25}O_4$	44.04	17.58	1.77
$Li_{0.25}Zn_{0.50}Fe_{2.25}O_4$ + 0.4 wt% V_2O_5	45.61	48.46	1.84
$Li_{0.25}Zn_{0.50}Fe_{2.25}O_4$ + 0.8 wt% V_2O_5	50.26	34.50	2.03
$Li_{0.25}Zn_{0.50}Fe_{2.25}O_4$ + 1.2 wt% V_2O_5	47.28	40.56	1.92

4.5 Complex Magnetic Permeability

The complex magnetic permeability spectra strongly depend on the sintered density, porosity and microstructure [22]. The permeability of the ferrites can be derived from the superposition of spin rotation and domain wall motion. The high magnetic permeability plays a crucial role due to the enhancement of the magnetic softness nature of the spinel ferrites. Therefore, it is necessary to improve the magnetic permeability from the applications point of view in the electromagnetic devices. The initial complex permeability is given by $\mu_i^* = \mu_i' - j\mu_i''$, where μ_i' and μ_i'' are denoted the real and imaginary parts of initial permeability, respectively. μ_i' indicates the stored energy expressing the component of magnetic induction B which is in phase with the alternating magnetic field H, while μ_i'' represents the dissipation of energy expressing the component of magnetic induction B which is out of phase with the alternating magnetic field H.

Fig. 4.8 Variation of μ_i' as a function of applied frequency for various $Li_{0.25}Zn_{0.50}Fe_{2.25}O_4 + xV_2O_5$ sintered at 1050 °C.

4.5.1 Frequency dependence of complex permeability

Fig. 4.8 depicts the variation of μ_i' with applied frequency for various $Li_{0.25}Zn_{0.50}Fe_{2.25}O_4 + xV_2O_5$ samples sintered at 1050 °C in the frequency range from 10 kHz-120 MHz at 300K. It is observed that μ_i' remains almost constant upto some critical frequency characterized by the onset of resonance, after a small rise, then curves drop rapidly at higher frequency. As a consequence, μ_i'' gradually increased with the applied frequency and shows a broad maximum in the higher frequency region. This behavior is shown for all the samples. This feature is called the ferrimagnetic resonance [82, 83].

Fig.4.9 shows the variation of μ_i'' with applied frequency. It can be seen that a sharp decrease of μ_i' is associated with the increase of μ_i''. The resonance frequency is due to the absorption of energy, which occurs when the applied frequency and the oscillation frequency of the magnetic dipoles are matching to each other. It is clearly observed that the value of μ_i' increases with the addition of V_2O_5 (upto 0.8 wt%), which could be attributed to promote of grain growth and densification of the samples or the reduction of porosity.

Fig. 4.9 Variation of μ_i'' as a function of applied frequency for various $Li_{0.25}Zn_{0.50}Fe_{2.25}O_4 + xV_2O_5$ sintered at 1050 °C.

Fig. 4.10 Variation of $tan\delta_M$ as a function of applied frequency for various $Li_{0.25}Zn_{0.50}Fe_{2.25}O_4 + xV_2O_5$ sintered at 1050 °C.

However, μ_i' was found to reduce for 1.2 wt% V_2O_5 which may be related to decrease in the grain size. Therefore, it clearly demonstrates that the magnetic permeability is closely related to the grain size of polycrystalline ferrite materials. It also displayed that the resonant frequencies were shifted towards the lower frequency from 16 to 10 MHz with the addition of V_2O_5 (upto 0.8 wt%) which expected according to Snoek's relation, $\mu_i' f_r$ = constant [84].

Generally, the complex permeability is derived from two different magnetizations mechanisms such as the domain wall motion and the spin rotational magnetization. The spin rotational component is of relaxation type in which the damping fraction is large enough and it dispersion is inversely proportional to the frequency, while the domain wall contribution is of resonance type and the dispersion of domain wall component depends on the square of the frequency [67]. The permeability (μ) can be expressed as

$$\mu(\omega) = 1 + \chi_{spin}(\omega) + \chi_{dw}(\omega) \tag{4.8}$$

where χ_{spin} is the susceptibility due to spin or rotational motion and χ_{dw} is the susceptibility due to domain wall motion. χ_{dw} and χ_{spin} can be written as follows

$$\chi_{dw} = \frac{3\pi M_s^2 D}{4\gamma} \tag{4.9}$$

$$\chi_{spin} = \frac{2\pi M_s^2}{K} \tag{4.10}$$

where K is the anisotropy constant and γ the domain wall energy. It is known that the permeability spectra of the polycrystalline ferrites are affected by sintered density, porosity and microstructural features. The domain wall motion strongly depends on the microstructure such as D. In the present study, it demonstrates that the initial permeability is strongly depended on D. Therefore, the increase of initial permeability with the addition of V_2O_5 could be attributed to the sintered density, larger grain size and reduced porosity. It is also noted that the intragranular pores might be responsible for the pinning of the domain walls in the higher frequency region, causing the magnetic permeability of Li-Zn ferrites to deteriorate. The frequency stability of μ_i' is an important factor from the applications point of view such as broad band transformer and wide band read-write head. It is observed that all the samples have shown the flat profile

in the permeability spectra of the polycrystalline Li-Zn ferrites with the addition of V_2O_5.

Fig. 4.10 shows the variation of $tan\delta_M$ as a function of applied frequency for various $Li_{0.25}Zn_{0.50}Fe_{2.25}O_4 + xV_2O_5$. It is observed that the value of $tan\delta_M$ is high at low frequency region, after a particular frequency, it remains almost constant. It is also observed that a rapid increase in $tan\delta_M$ is found at higher frequency region. It has been demonstrated that the phase lag between domain rotation and applied field is larger than that of domain wall movement. Magnetic loss arises when domain rotation dominates compared with domain wall movement [7].

4.5.2 Relative quality factor

Fig. 4.11 Variation of RQF as a function of applied frequency for various $Li_{0.25}Zn_{0.50}Fe_{2.25}O_4 + xV_2O_5$ sintered at 1050 °C.

The relative quality factor (RQF) is used as a measure of performance from the application point of view. The variation of RQF of various $Li_{0.25}Zn_{0.50}Fe_{2.25}O_4 + xV_2O_5$ samples with the applied frequency is shown in Fig. 4.11. It is shown that the RQF increases with the increase in frequency and showing a peak, after that it decreases with

further increase in frequency. This behavior is clearly shown for all the samples. It demonstrates that the enhancement of RQF is evidenced on V_2O_5 addition. The peak positions of RQF are shifted to lower frequencies as the amount of V_2O_5 addition, which is associated with Snoek's law. The sample for 0.8 wt% V_2O_5 possesses the maximum value of RQF which could be attributed to the larger grain size and densification of the materials in compared to other compositions. On the other hand, the wider/broader frequency band is found to be observed for pure $Li_{0.25}Zn_{0.50}Fe_{2.25}O_4$ system, while the frequency band is less wider or narrower to be observed for V_2O_5 added Li-Zn ferrites samples due to larger value of RQF. It can be concluded that V_2O_5 added Li-Zn ferrites samples are performed with tiny magnetic power losses.

4.6 Electrical Properties

4.6.1 Dielectric constant and loss factor

Fig 4.12 Variation of ε' with applied frequency for various $Li_{0.25}Zn_{0.50}Fe_{2.25}O_4 + xV_2O_5$ sintered at 1050 °C.

Fig 4.12 shows the frequency dependent dielectric constant (ε') at room temperature for $Li_{0.25}Zn_{0.50}Fe_{2.25}O_4$ + xV_2O_5 samples, where (0.0, 0.4, 0.8 and 1.2 wt%). It is seen that ε' decreases with increasing of frequency and attains a constant value. The dielectric property of the sample follows Maxwell-Wagner type interfacial polarization [85]. The higher value of ε' was observed at the lower frequency region which may be related to the dominant role of the interfacial polarization, while the lower value of ε' was found at the high frequency region which could be attributed to the weaker role of the interfacial and dipolar polarization. Ferrites contain well conducting grains separated by poorly conducting grain boundaries. At high frequencies, the ferrites grain is more efficient, while the grain boundaries are more effective at low frequency. At lower frequencies, the charge carriers are easily accumulated at the grain boundaries. These accumulated charges take part in polarization, which leads to high permittivity of the materials. It can also be seen from Fig. 4.12 that the dielectric constant of V_2O_5 added Li-Zn ferrites are larger than that of pure Li-Zn ferrites.

Fig 4.13 Variation of ε'' with applied frequency for various $Li_{0.25}Zn_{0.50}Fe_{2.25}O_4$ + xV_2O_5 sintered at 1050 °C.

Fig 4.13 shows the frequency dependent imaginary part of dielectric constant (ε'') at room temperature for $Li_{0.25}Zn_{0.50}Fe_{2.25}O_4$ + xV_2O_5 samples. It is observed that the

variation of ε'' with frequency displays similar behavior as real part (ε') of dielectric constant. It is well known that polarizations of the samples are depended on several factors such as sintered density, microstructure and porosity of the ferrites [86]. The increase of densification of V_2O_5 added Li-Zn ferrites are contributing to enhance the polarization resulting in higher dielectric constants at lower frequency region. It is also found that the rate of change of dielectric constant with frequency of V_2O_5 added samples clearly displays slow decreasing trend compared with pure Li-Zn ferrites at higher frequency, which indicates that V_2O_5 added samples display frequency stability than that of pure system. According to Verwey and de Boer, the electronic exchange ($Fe^{2+} \leftrightarrow Fe^{3+}$) occurs at the crystallographic equivalent site without any change of the energy state of the crystal resulting in transition [87]. The frequency dependency of ε' can also be explained with the hopping mechanism at the octahedral site of spinel ferrites. The hopping frequency of electrons cannot follow the applied ac field at the higher frequency region. This is because the electron exchange interaction $Fe^{2+} \Leftrightarrow Fe^{3+}$ cannot follow the applied field due to the phase delay to line up their axes parallel with the field direction. Therefore the dielectric constant becomes low and attains a constant value for all the samples.

Fig. 4.14 Variation of $tan\delta_E$ with applied frequency for various $Li_{0.25}Zn_{0.50}Fe_{2.25}O_4$ + xV_2O_5 sintered at 1050 °C.

The dielectric loss is the inherent dissipation of electromagnetic energy as a form of heat. There are two types of loss in a dielectric medium. i) The energy dissipation caused by flowing of charge through a material is called the conduction loss. ii) In dielectric loss, the dissipation of energy caused by the movement of charges in an alternating electromagnetic field as polarization switches direction. Fig. 4.14 shows the variation of dielectric loss factor ($tan\delta_E$) with applied frequency. It is observed that the dielectric material follows Debye relaxation theory [70].

Iwauchi [88] pointed that there is relation between the dielectric property and conduction mechanism of ferrites. Conduction mechanism is considered as the hopping of electrons between Fe^{2+} and Fe^{3+} ions due to n-types ferrites. $tan\delta_E$ is maximum when the relation $\omega\tau = 1$ is satisfied, where $\omega = 2\pi f_o$ and τ is the relaxation time, and f_o is the resonance frequency. Thus, the value of $tan\delta_E$ is maximum when the hopping frequency of electron is approximately equal to the applied frequency. This is due to the effect of ferrimagnetic resonance. The value of $tan\delta_E$ displays small value which occurs due to the activity of conducting grains at higher frequencies. The higher value of $tan\delta_E$ at lower frequency region is observed due to the grain boundary effect which requires more energy for the exchange of electron between Fe^{2+} and Fe^{3+} ions. The lower value of $tan\delta_E$ is observed at the higher frequency region, which could be related to the inability of domain wall motion with the rapid variation of applied ac field [89]. The lower dielectric losses of V_2O_5 added Li-Zn ferrites observed at higher frequencies may open an avenue for the possible application in high frequency devices.

4.6.2 Ac resistivity and conductivity

Fig. 4.15 shows the variation of ac electrical resistivity (ρ_{ac}) with the applied frequency. It shows that ρ_{ac} decreases continuously with increasing of frequency and becomes a constant value at higher frequency range. It is also observed from Fig. 4. 12 that ε' and ρ_{ac} due to the addition of V_2O_5 content in Li-Zn ferrites are in inverse relationship to each other, which shows the normal trend of ferrites. The electrical resistivity of V_2O_5 added Li-Zn ferrites at a selected frequency (100Hz) are shown in Table 4.6. It clearly shows that the resistivity was found to decrease with the amount of V_2O_5 content (from 0.0 to 0.8 wt%) which could be attributed to the enhancement of grain size in the samples.

Fig. 4.15 Variation of ρ_{ac} with applied frequency of various $Li_{0.25}Zn_{0.50}Fe_{2.25}O_4$ + xV_2O_5 sintered at 1050 °C.

Table 4.6 Electrical resistivity of $Li_{0.25}Zn_{0.50}Fe_{2.25}O_4$ at 100 Hz for different content of V_2O_5.

V_2O_5-content (wt%)	ρ_{ac} (MΩ-m)
0.0	2.50
0.4	1.33
0.8	1.17
1.2	1.87

The hopping of electrons takes place at the octahedral site (B-site) and the amount of iron (Fe^{3+}) ions is mainly responsible for the hopping of electronic exchange between the localized sites. The conductivity of ferrites is given as, $\sigma_{ferrite} = \sigma_{dc} + \sigma_{ac}(\omega)$ where σ_{dc} represents the dc conductivity and σ_{ac} indicates the frequency dependent term, known as the ac conductivity [90]. The variation of ac conductivity (σ_{ac}) as a function of frequency at room temperature is shown in Fig. 4.16. It is observed that at

low frequency region, the conductivity almost remains constant because the resistive grain boundaries are much more effective than highly conducting grains. As a consequence, the electrons jumping frequency between Fe^{2+} and Fe^{3+} ions become low and insignificant in the low frequency region. While at higher frequencies, it increases rapidly with the applied frequency due to the activity of conductive grain. This is because the high electrical conductivity of grains is more active than poor conducting grain boundaries. Therefore, the enhancement of conductivity could be attributed to increase of hopping of electrons between Fe^{2+} and Fe^{3+} ions due to the activity of grains of the samples in higher frequency region. It is also found that the increase of conductivity of V_2O_5 added Li-Zn ferrites may also be related to the densification and larger grain size of the samples.

According to Jonscher's power law [91], the total conductivity is given by

$$\sigma_{total}(\omega) = \sigma_{dc} + B\omega^n \qquad (4.11)$$

where $\omega(= 2\pi f)$ is the frequency, n is the dimensionless exponent quantity, which gives the information about the conduction mechanism of the samples, $B\omega^n$ represents the ac conductivity term due to hopping process at the octahedral site [90].

Fig. 4.16 Variation of σ_{ac} with applied frequency of various $Li_{0.25}Zn_{0.50}Fe_{2.25}O_4$ + xV_2O_5 sintered at 1050 °C.

Fig. 4.17 Variation of $\log\sigma_{ac}$ with $\log(\omega)$ of various $Li_{0.25}Zn_{0.50}Fe_{2.25}O_4 + xV_2O_5$ sintered at 1050 °C.

Fig. 4.17 shows relation between $\log\sigma_{ac}$ and $\log\omega$ for all the samples at room temperature. The value of n can be obtained from the slope of the $\log\sigma_{ac}$ *vs* $\log\omega$. It is found to be in the range $0 < n < 1$ which confirms that the conduction of the samples is dependent on the frequency [92]. According to Jonscher's power law, the variation of $\log\sigma_{ac}$ with $\log\omega$ should be linear relation. However, the conductivity of the samples shows a slightly deviation of linear line at the low frequency region due to mixed polaron hopping. But, it shows that the conductivity increases with linear fashion in the higher frequency region, which could be attributed to the small polaron hopping [89]. Therefore, the enhancement of the electrical conductivity is clearly demonstrated with hopping conduction mechanism.

4.6.3 Electric Modulus Spectra analysis

Electric modulus study is an essential method to measure electrical properties (conductivity, relaxation time, ion or charge carrier hopping rate, etc.) in the materials. It also provides an alternative approach to analyze the electrical response of the

materials. It is associated with energy-giving to the system and dissipation from it during the conduction process.

Fig. 4.18 Real part of electric modulus spectra with applied frequency of various $Li_{0.25}Zn_{0.50}Fe_{2.25}O_4 + xV_2O_5$ sintered at 1050 °C.

Macedo *et al.* [93] studied the electrical relaxation in the term of dielectric modulus (M*) given by

$$M^*(\omega) = \frac{1}{\varepsilon^*} = \frac{1}{\varepsilon' - j\varepsilon''} = \frac{\varepsilon'}{\varepsilon'^2 + \varepsilon''^2} + j\frac{\varepsilon''}{\varepsilon'^2 + \varepsilon''^2}$$

$$= M'(\omega) + jM''(\omega) \tag{4.12}$$

Simplifying and substituting ε'' by $\varepsilon' tan\delta_E$, we get

$$M^*(\omega) = M'(\omega) + jM''(\omega)$$

$$= \frac{1}{\varepsilon'(1+tan^2\delta_E)} + j\frac{tan\delta_E}{\varepsilon'(1 + tan^2\delta_E)} \tag{4.13}$$

where M' and M'' are the real and imaginary parts of M^* and these M' and M'' are calculated from ε' and ε''.

Fig. 4.19 Imaginary part of electric modulus spectra with applied frequency of various $Li_{0.25}Zn_{0.50}Fe_{2.25}O_4 + xV_2O_5$ sintered at 1050 °C.

Fig. 4.18 shows the change of real part (M') of the electric modulus with frequency. It is observed that the value of M' is almost zero in the low frequency region, indicates the presence of significant electrode or ionic polarization in the Li-Zn ferrites. Because of the short range mobility of charge carriers, the dispersion is displayed in the high frequency region. This result possibly related to the shortage of restoring force controlling the mobility of charge carriers under the influence of an applied electric field [94]. It is also observed that the value of M' is increased with V_2O_5 addition. Fig. 4.19 indicates the variation of imaginary part (M'') of dielectric modulus with frequency. It is seen that M'' increases with frequency in the low frequency area and displays a relaxation peak. In the high frequency region, M'' decreases with frequency and becomes almost merge due to limited carriers in potential wells. The low frequency region determines the range in which way charge carriers are mobile over long distances allowing between the grains. At frequencies above the peak, the carriers are spatially confined to their potential wells, having mobile over short distances allowing within the grains [66]. The observed peaks shift toward the higher frequencies with ferrite content, indicating the mobility of carriers is from long to short range with the frequency

increases, [7]. The asymmetry in peak broadening refers to the presence of different relaxation times that imply the non-Debye type of relaxation and confirms the presence of the hopping mechanism of electrical conduction.

4.6.4 Impedance spectroscopy

Fig. 4.20 Variation of Z' with applied frequency of various $Li_{0.25}Zn_{0.50}Fe_{2.25}O_4 + xV_2O_5$ sintered at 1050 °C.

The measurement of impedance is a significant factor in order to get the knowledge about the electrical transport mechanism of $Li_{0.25}Zn_{0.50}Fe_{2.25}O_4 + xV_2O_5$ samples. The complex impedance gives the information about the resistive (Z') and reactive (Z'') components of the samples. In order to study of the electrical conduction mechanism of the samples, the complex impedance measurement was carried out as function of frequency. Fig. 4.20 shows the variation of Z' with applied frequency of various $Li_{0.25}Zn_{0.50}Fe_{2.25}O_4 + xV_2O_5$ samples. It is observed that Z' gradually decreases with the increase of frequency, which indicates that ac conductivity increases with applied frequency for all the samples. The Variation of Z'' with applied frequency of various $Li_{0.25}Zn_{0.50}Fe_{2.25}O_4 + xV_2O_5$ is shown in Fig. 4. 21. It shows dispersion due to the presence of space charge relaxation behavior in the material. The frequency independent

nature of Z' and Z'' are observed at higher frequencies, which may be related to the reduction of space charge polarization at the grain boundaries [95].

Fig. 4.21 Variation of Z'' with applied frequency of various $Li_{0.25}Zn_{0.50}Fe_{2.25}O_4$ + xV_2O_5 sintered at 1050 °C.

4.6.5 Cole-Cole plot

In order to study of the influence of grain and grain boundary on the electrical properties of $Li_{0.25}Zn_{0.50}Fe_{2.25}O_4+xV_2O_5$, Cole-Cole plots ($Z''vs$ Z') have been investigated for all the samples. Polycrystalline materials can be represented as an equivalent circuit consists of three parallel RC circuits connected in series, which can explain the relaxors properties of the material having the effect of grains, grain boundaries and surface electrode, respectively [64].

Each RC element of the equivalent circuit makes a semicircle. According to the equivalent circuit, impedance (Z^*) can be written as [89]

$$Z^* = R_g - \frac{1}{j\omega_g C_g} + R_{gb} - \frac{1}{j\omega_{gb} C_{gb}} \qquad (4.14)$$

where R_g and R_{gb} are the grain and grain boundary resistances, C_g and C_{gb} are grain and grain boundary capacitances, respectively, while ω_g and ω_{gb} are the frequencies at the peak of semicircle for grain and grain boundary, respectively.

Fig. 4.22 Cole-Cole plot of various $Li_{0.25}Zn_{0.50}Fe_{2.25}O_4 + xV_2O_5.$

Cole-Cole plots indicated the contribution of grain and grain boundary to the total resistance of the sample [70]. Fig. 4.22 depicts the Cole-Cole plot for various $Li_{0.25}Zn_{0.50}Fe_{2.25}O_4 + xV_2O_5$ samples.

Fig. 4.23 indicates Cole-Cole plots of various $Li_{0.25}Zn_{0.50}Fe_{2.25}O_4 + xV_2O_5$ with fitting. From the Nyquist plot, it is observed that all samples have shown a single semicircular arc. A single semicircle arcs represent only one primary mechanism is responsible for the conduction in the present study. Partial semicircles are found to be observed in all the samples. Non-Debye type relaxation is observed due to its distorted semi-circle. It is also observed that the areas of the semicircle are reduced for V_2O_5 added Li-Zn ferrites than that of Li-Zn ferrites which could be attributed to the decrease of resistance resulting in higher conductivity of V_2O_5 added Li-Zn ferrites samples compared to Li-Zn ferrites. It can be concluded that the semicircular arc corresponding to the conduction due to the grain in the high frequency region, which could be attributed to

the large grain sizes in V_2O_5 added Li-Zn ferrites [89]. Therefore, the conduction might take place through the grain.

Fig. 4.23 Cole-Cole plots of various $Li_{0.25}Zn_{0.50}Fe_{2.25}O_4 + xV_2O_5$; experimental data (black line), fitting data (red line).

CHAPTER 5

CONCLUSIONS

5.1 Summary

The XRD diffraction patterns confirmed that all the samples have shown single phase cubic spinel structure.

The bulk density was increased from 4.30 g/cm^3 for (x = 0.0) to 4.51 g/cm^3 for (x = 0.8 wt%), while the porosity decreases as the addition of V_2O_5 content up to an optimum concentration.

The microstructural studies showed that the grain growth of Li-Zn ferrites is strongly depended on V_2O_5 addition. The average grain sizes were increased from 5.3 (for x = 0.0 wt%) to 7.7μm (for x = 0.8 wt% V_2O_5), which could be attributed to the role of V_2O_5 as sintering aid to enhance the densification of the samples.

EDS spectrum indicates the existence of Zn, Fe, V and O elements. Li is not detectable by the machine due to its light weight. As provided by the EDS spectrum, the concentration of these components matches the ferrite structure fairly.

The magnetic hysteresis analysis demonstrated that the saturation magnetizations were increased from 44.0 (for x = 0.0 wt%) to 50.3 emu/g (for x = 0.8 wt% V_2O_5). However, the saturation magnetization was found to decrease for x = 1.2 wt% V_2O_5, which may be related to weaken of exchange interaction due to the introduction of excess non-magnetic V_2O_5.

The complex initial magnetic permeability has been studied and it shows that the enhancement of the permeability is clearly evidenced on V_2O_5 addition, which could be attributed to promote of grain growth and densification of the samples or the reduction of porosity.

The dielectric constants of V_2O_5 added Li-Zn ferrites are larger than that of pure Li-Zn ferrites. The increase of densification of V_2O_5 added Li-Zn ferrites are contributing to enhance the polarization resulting in higher dielectric constants at lower frequency region.

Frequency dependent electrical conductivity measurement demonstrated that the enhancement of conductivity could be attributed to increase of hopping of electrons between Fe^{2+} and Fe^{3+} ions due to the activity of grains in higher frequency region. It is also found that the increase of conductivity of V_2O_5 added Li-Zn ferrites may also be related to the densification and larger grain size of the samples.

The complex impedance spectroscopy through Cole-Cole plot has demonstrated a single semicircular arc, which indicates that conduction mechanism takes place predominantly through the grain property.

5.2 Conclusions

In this study, the compactness of Li-Zn ferrites is obtained with the addition of V_2O_5 sintered at 1050 ºC. The effects of V_2O_5 additive on morphology and electromagnetic properties of the low sintered Li-Zn ferrites have been discussed in detail. The XRD results have indicated that adding a small amount of V_2O_5 (less than 1.2 wt%) had no apparent influence on spinel phase Li-Zn ferrites. The bulk density increased and porosity decreased up to the optimum V_2O_5 content at x = 0.8 wt%, and beyond that level, ρ_B decreased and P increased. The average grain size is maximum at 0.8 wt% V_2O_5 content and then slightly deteriorated. This result executed the high initial permeability and high saturation magnetization of Li-Zn ferrites. The changes of ε' with frequency have displayed the usual dielectric dispersion. Both modulus and conductivity have exhibited polaron hopping type of conduction. Impedance spectroscopy measurement demonstrated that the composites have only a grain effect on electrical properties. The Cole-Cole plots have indicated that the resistance of the samples decreased with V_2O_5 content and showed non-Debye type relaxation. The lower value of dielectric loss for V_2O_5 added Li-Zn ferrites indicates that it may open an avenue for the possible application in high frequency devices.

5.3 Suggestions for the Future Work

Further investigations on different aspects are possible for fundamental interest and potential applications of the studied ferrite. Following recommendations are made for further extension of the present work:

- Mössbauer spectroscopy can be performed to know the cation distribution.

- In order to know the T_C, M-T measurement may be performed for the prepared samples.

Reference

[1]   Ghodake, U. R., Kambale, R. C., and Suryavanshi, S. S., "Effect of Mn^{2+} substitution on structural, electrical transport and dielectric properties of Mg-Zn ferrites", *Ceram. Int.*, vol. 43, pp. 1129-1134, 2017.

[2]   Raju, K., Venkataiah, G., and Yoon, D. H., "Effect of Zn substitution on the structural and magnetic properties of Ni-Co ferrites", *Ceram. Int.,* vol. 40, pp. 9337–9344, 2014.

[3]   Akhter, S., Paul, D. P., Hoque, S. M., Hakim, M.A., Hudl, M., Mathieu, R., and Nordblad, P., "Magnetic and magnetocaloric properties of $Cu_{1-x}Zn_xFe_2O_4$ (x = 0.6, 0.7, 0.8) ferrites", *J. Magn. Magn. Mater.*, vol. 367, pp. 75-80, 2014.

[4]   Harun-Or-Rashid, M., Islam, M. N., Arifuzzaman, M., and Hossain, A. K. M. A., "Effect of sintering temperature on the structural, morphological, electrical, and magnetic properties of Ni–Cu–Zn and Ni–Cu–Zn–Sc ferrites", *J. Mater. Sci.: Mater. Electron.*, vol. 3, pp. 2505-2523, 2021.

[5]   Islam, M., Jhahan, M., Khatun, M. T., Khan, M. N. I., Rahman, M. J., Al-Momin, A., and Alam, M. M., "Influence of Mg substitution on structural, magnetic and electrical properties of Zn-Cu ferrites." *J. Mater. Sci.: Mater. Electron.*, vol. 297, pp. 1-8. 2021.

[6]   Anupama, A. V., Manjunatha, M., Rathod, V., Jali, V. M., Damle, R., Ramesh, K.P., and Sahoo, B., "^{57}Fe internal field nuclear magnetic resonance and Mössbauer spectroscopy study of Li-Zn ferrites" , *J. Magn. Reson.*, vol. 286, pp. 68-77, 2018.

[7]   Das, B. C, Alam, F., and Akther, A. K. M. A., "The crystallographic, magnetic, and electrical properties of Gd^{3+}-substituted Ni–Cu–Zn mixed ferrites*", J. Phys. Chem. Solids.*, vol. 142, p. 109433, 2020.

[8]   Sharif, M., Jacob, J., Javed, M., Manzoor, A., Mahmood, K., and Khan, M. A., "Impact of Co and Mn substitution on structural and dielectric properties of lithium soft ferrites", *Phys. Rev. B Condens. Matter.*, vol. 567, pp. 45-50, 2019.

[9]   Singh, N., Agarwal, A., Sanghi, S., and Khasa, S., "Dielectric loss, conductivity relaxation process and magnetic properties of Mg substituted Ni–Cu ferrites", *J. Magn. Magn. Mater.*, vol. 324, pp. 2506-2511, 2012.

[10]   Gao, Y., Wang, Z., Shi, R., Pei, J., Zhang, H., and Zhou, X., "Electromagnetic and microwave absorption properties of Ti doped Li–Zn ferrites", *J. Alloys Compd.,* vol. 805, pp. 934-941, 2019.

[11]   Singh, N., Agarwal, A., and Sanghi, S., "Dielectric relaxation, conductivity behavior and magnetic properties of Mg substituted Zn–Li ferrites", *Curr. Appl. Phys.*, vol. 11, pp. 783-789, 2011.

[12] Rathod, V., Anupama, A. V., Jali, V. M., Hiremath, V. A., and Sahoo, B., "Combustion synthesis, structure and magnetic properties of Li-Zn ferrite ceramic powders", *Ceram. Int.*, vol. 43, pp. 14431-14440, 2017.

[13] Fazio, E. D., Bercoff, P. G., and Jacobo, S. E., "Electromagnetic properties of manganese–zinc ferrite with lithium substitution", *J. Magn. Magn. Mater.*, vol. 323, pp. 2813-2817, 2011.

[14] Anupama, A. V., Rathod, V., Jali, V. M., and Sahoo, B., "Composition dependent elastic and thermal properties of LiZn ferrites" *J. Alloys Compd.*, vol. 728, pp. 1091-1100, 2017.

[15] Kavanloui, M., and Hashemi, B., "Effect of B_2O_3 on the densification and magnetic properties of Li–Zn ferrite", *Mater. Des.,* vol. 32, pp. 4257-4261, 2011.

[16] Anupama, A.V., Kumaran, V., and B. Sahoo, "Magnetorheological fluids containing rod shaped lithium–zinc ferrite particles: the steady-state shear response", *Soft Matter*, vol. 14, pp. 5407–5419, 2018.

[17] Gao, Y., Wang, Z., Pei, J., and Zhang, H., "Structural, elastic, thermal and soft magnetic properties of Ni-Zn-Li ferrites", *J. Alloys Compd.*, vol. 774, pp. 1233-1242, 2019.

[18] Nakamura, T., Miyamoto, T., and Yamada, Y., "Complex permeability spectra of polycrystalline Li–Zn ferrite and application to EM-wave absorber", *J. Magn. Magn. Mater.*, vol. 256 pp. 340–347 2003.

[19] Soibam, I., Phanjoubam, S., Sharma, H.B., Sarma, H. N. K., and Prakash, C., "Magnetic studies of Li–Zn ferrites prepared by citrate precursor method", *Phys. Rev. B Condens. Matter.*, vol. 404, pp. 3839-3841, 2009.

[20] Darwish, M. A., Saafan, S. A., El-Kony, D., and Salahuddin, N. A., "Preparation and investigation of dc conductivity and relative permeability of epoxy/Li–Ni–Zn ferrite composites", *J. Magn. Magn. Mater.,* vol. 385, pp. 99-106, 2015.

[21] Manzoor, A., Khan, M. A., Khan, M. Y., Akhtar, M. N., and Hussain, A., "Tuning magnetic and high frequency dielectric behavior in Li-Zn ferrites by Ho doping", *Ceram. Int.*, vol. 44, pp. 6321-6329 2018.

[22] Nasrin, S., Khan, S. M., Matin, M. A., Khan, M. N. I., Hossain, A. K. M. A., and Rahaman, M. D., "Synthesis and deciphering the effects of sintering temperature on structural, elastic, dielectric, electric and magnetic properties of magnetic $Ni_{0.25}Cu_{0.13}Zn_{0.62}Fe_2O_4$ ceramics", *J. Mater. Sci.: Mater. Electron.,* vol. 30, pp. 10722-10741. 2019.

[23] Gore, S. K., Jadhav, S. S., Jadhav, V. V., Patange, S. M., Naushad, M., Mane, R. S., and Kim, K. H., "The structural and magnetic properties of dual phase cobalt ferrite", *Sci. Rep.,* vol. 7, p. 2524, 2017.

[31] Hu, J., Shi, G., Ni, Z., Zheng, L., and Chen, A., "Effects of V_2O_5 addition on NiZn ferrite synthesized using two-step sintering process", *Physica B*, vol. 407, pp. 2205–2210, 2012.

[32] Liao, Y., Xu, F., Zhang, D., Zhou, T., Wang, Q., Wang, X., Jia, L., Li, J., Su, H., Zhong, Z., and Zhang, H., "Low Temperature Firing of $Li_{0.43}Zn_{0.27}Ti_{0.13}Fe_{2.17}O_4$ Ferrites with Enhanced Magnetic Properties", *J. Am. Ceram. Soc.*, vol. 98, pp. 2556–2560, 2015.

[24] Xua, F., Shi, X., Liao, Y., Li, J., and Hu, J., "Investigation of grain growth and magnetic properties of low-sintered LiZnTi ferrite-ceramic", *Ceram. Int.,* vol. 46, pp. 14669–14673 2020.

[25] Chengyong, L., Lan, Z., Jiang, X., Yu, Z. Sun, K., Li, L., and Liu, P., "Effects of sintering temperature and Bi_2O_3 content on microstructure and magnetic properties of LiZn ferrites", *J. Magn. Magn. Mater.*, vol. 320, pp. 1335–1339 2008.

[26] Lebourgeois, R., Duguey, S., Ganne, J. P., and Heintz, J. M., "Influence of V_2O_5 on the magnetic properties of nickel–zinc–copper Ferrites" *J. Magn. Magn. Mater.,* vol. 312, pp. 328–330 2007.

[27] Mahmoudi, M., and Kavanlouei, M., "Temperature and frequency dependence of electromagnetic properties of sintering Li–Zn ferrites with nano SiO_2 additive", *J. Magn. Magn. Mater.*, vol. 384, pp. 276-283 2015.

[28] Wang, X., Zhang, D, Wang, G., Jin, L., Li, J, Liao, Y., Zhang, H., and Wang, S., "Synthesis of V_2O_5-Doped and low-sintered NiCuZn ferrite with uniform grains and enhanced magnetic properties", *Ceram. Int.*, vol.46, pp. 10652–10657, 2020.

[29] Mirzaee, O., Golozar, M. A., and Shafyei, A., "Influence of V_2O_5 as an effective dopant on the microstructure development and magnetic properties of $Ni_{0.64}Zn_{0.36}Fe_2O_4$ soft ferrites," *Mater. Charact.*, vol. 59, pp. 638-641, 2008.

[30] Janghorban, K., and Shokrollahi, H., "Influence of V_2O_5 addition on the grain growth and magnetic properties of Mn-Zn high permeability ferrites", *J. Magn. Magn. Mater.,* vol. 308, pp. 238-242, 2007.

[31] Hu, J., Shi, G., Ni, Z., Zheng, L., and Chen, A., "Effects of V_2O_5 addition on NiZn ferrite synthesized using two-step sintering process", *Physica B*, vol. 407, pp. 2205–2210, 2012.

[32] Liao, Y., Xu, F., Zhang, D., Zhou, T., Wang, Q., Wang, X., Jia, L., Li, J., Su, H., Zhong, Z., and Zhang, H., "Low temperature firing of $Li_{0.43}Zn_{0.27}Ti_{0.13}Fe_{2.17}O_4$ ferrites with enhanced magnetic properties", *J. Am. Ceram. Soc.*, vol. 98, pp. 2556–2560, 2015.

[33] Ullah, M. S., Uddin, M. F., Momin, A. A., and Hakim, M. A., "Effect of V_2O_5 addition on the structural and magnetic properties of Ni–Co–Zn ferrites", *Mater. Res. Express.*, vol. 8, p. 016102, 2021.

[34] Xu, F., Zhang, H., Xie, F., Liao, Y., Li, Y., Li J., Jin, L., Yang, Y., Gan, G., Wang, G., and Zhao Q., "Investigation of grain boundary diffusion and grain growth of lithium zinc ferrites with low activation energy", *J. Am. Ceram. Soc.,* vol. 101, pp. 5037-5045, 2018.

[35] Kaiser, M., "Influence of V_2O_5 ion addition on the conductivity and grain growth of Ni-Zn-Cu ferrites", *Curr. Appl. Phys..,* vol. 10, pp. 975-984, 2010.

[36] Zhang, L., Wang, Y., Liu, B., Wang, J., Han, G., and Zhang, Y., "Characterization and property of magnetic ferrite ceramics with interesting multilayer structure prepared by solid-state reaction", *Ceram. Int*., vol. 47, pp. 10927-10939, 2021.

[37] Madhuri, W., and Naidu, C. B., "Microwave assisted solid state reaction method: investigations on electrical and magnetic properties NiMgZn ferrites", *Mater. Chem. Phys.*, vol. 181, pp. 432-443, 2016.

[38] Rao, B. P., Caltun, O., Dumitru, I., and Spinu, L. "Complex permeability spectra of Ni-Zn ferrites doped with V_2O_5/Nb_2O_5", *J. Magn. Magn. Mater*., vol. 308, pp. 238-242, 2007.

[39] Mirzaee, O., Shafyei, A., and Shokrollahi, H., "Influence of MoO_3 and V_2O_5 co-doping on the magnetic properties and microstructure of a Ni-Zn ferrite", *J. Alloys Compd.,* vol. 461, pp. 312-315, 2008.

[40] M. A. Wahab (1999) *Solid State Physics: Structure and Properties of Materials*, Narosa Publishing House, New Delhi.

[41] Goldman, A. (1999) *Handbook of Modern Ferromagnetic Materials*, Kulwer Acad. Pub, Boston, U.S.A.

[42] Cullity, B.D. (1972) *Introduction to Magnetic Materials*, Addison-Wisley Publishing Company, Inc., California.

[43] Valenzuela, R. (1994) *Magnetic Ceramics*, Cambridge University Press, Cambridge.

[44] Brailsford, F. (1996) *Physical Principles of Magnetism*, D. van Nostrand Company Ltd., London.

[45] Uddin, F., "Effect of V_2O_5 addition on the structural, magnetic and electrical properties of Ni-Co-Zn ferrites. M.Sc. Thesis, Department of Physics, Bangladesh University of Engineering and Technology, 2020.

[46] Jiles, D.C. and Atherton, D.L., "Theory of ferromagnetic hysteresis", *J. Magn. Magn. Mater.*, vol. 61, pp.48-60, 1986.

[47] Prodromakis, T., Application of Maxwell-Wagner Polarization in Monolithic Technologies, pp. 25-26, 2008.

[48] Prodromakis, T. and Papavassiliou, C., "Engineering the Maxwell–Wagner polarization effect", *Appl. Surf. Sci.,* vol. 255, pp. 6989-6994, 2009.

[49] Hill, N. E., Yaughan, W. E., Price, A. H., and Davis, M. (1969) *Dielectric properties and Molecular Behavior*, Van Nostrand, London.

[50] Böttcher, J .F., and Bordewijk, P. (1992) *Theory of Electric Polarisation*, vol. 2, second edition, Elsevier Science B. V., Amsterdam.

[51] Ahmad, Z., "Polymer dielectric materials", In Dielectric material, IntechOpen, 2012.

[52] Bahgat, M., Farghaly, F. E., Basir, S. M. A., and Fouad, O. A, "Synthesis, characterizatio and magnetic properties of microcrystalline lithium cobalt ferrite from spent lithium-ion batteries", *J. Mater. Process. Technol*., vol. 183, pp. 117–121, 2007.

[53] Battez, A. H., González, R., Viesca, J. L., Fernández, J. E., Fernández J. M. D., Machado, A., Chou, R., and Riba, J., " CuO, ZrO_2 and ZnO nanoparticles as antiwear additive in oil lubricants", *Wear*., vol. 265, pp. 422–428, 2008.

[54] Wu, W., He, Q., and Jiang, C., "Magnetic Iron Oxide Nanoparticles: Synthesis and Surface Functionalization Strategies", *Nanoscale Res. Lett.,* vol. 3, p. 397, 2008.

[55] Bauer, G., Güther, V., Hess, H., Otto, A., Roidl, O., Roller, H., and Sattelberger, S., "Vanadium and Vanadium Compounds", Ullmann's Encyclopedia of Industrial Chemistry, 2000.

[56] Shah, M. R., "dielectric properties of alkaline earth (D = Ba, Sr, Ca) and rare earth (T= La, Nd) substituted polycrystalline $D_{1-x}T_x(T_{0.5}Fe_{0.5})O_3$ pervoskite", Ph. D. Thesis, Department of Physics, Bangladesh University of Engineering and Technology, 2013.

[57] Hossain, A. K. M. A., "Investigation of colossal magneto resistance in bulk and thick film magnetites", Ph. D. Thesis, Impiral College, London, 1998.

[58] Brooks, R. J., Sintering: An Overview, Concise Encyclopedia of Advanced Ceramic Materials, Pergamon press, Oxford, p. 438, 1998.

[59] Reijnen, P., Science of Ceramics, Academic Press, London, 1967.

[60] Slick, P. I. (1980*) Ferrites for Non-microwave Applications*, vol. 2, North Holland Pub. Co., Netherlands.

[61] Epp. J., "4-X-ray diffraction (XRD) Techniques for Materials characterization", Foundation Institute of Materials Science, Germany, pp. 81-124, 2016.

[62] Mazen, S. A., and Dawoud, H. A., "Structure and Magnetic Properties of Li-Cu ferrites", Phys. Stat. sol., vol. 172, pp. 275-289, 1999.

[63]   Chikazumi, S. (1966) *Physics of Magnetism*, Jhon Wiley & Sons, Inc., New York.

[64]   MacDonald, J. R., "Impedance Spectroscopy", Wiley-Interscience, New York, 1987.

[65]   Prabu, M., and Selvasekarapandian, S., "Dielectric and modulus studies of LiNiPO$_4$", Mater. Chem. Phys., vol. 134, pp. 366–370, 2012.

[66]   Yin, Q., Liu, Y., Liu, Q., Wang, Y., Chen, J., Wang, H., Wu, C., and Zhang, H., "Study of the microstructure and microwave magnetic characteristics of Ti-doped Li–Zn ferrite", *J. Mater. Sci.: Mater. Electron.,* vol. 30, pp. 5430-5437, 2019.

[67]   Hossain, A. K. M. A., Mahmud, S. T., Seki, M., Kawai, T., and Tabata, H., "Structural, electrical transport, and magnetic properties of Ni$_{1-x}$Zn$_x$Fe$_2$O$_4$", *J. Magn. Magn. Mater.*, vol. 312, pp. 210-219, 2007.

[68]   Yadav, R. S., Kuřitka, I., Vilcakova, J., Urbánek, P., Machovsky, M., Masař, M., and Holek, M., "Structural, magnetic, optical, dielectric, electrical and modulus spectroscopic characteristics of ZnFe$_2$O$_4$ spinel ferrite nanoparticles synthesized via honey-mediated sol-gel combustion method", *J. Phys. Chem. Solids.*, 110, pp. 87-99, 2017.

[69]   Fawzi, A. S., Sheikh, A. D., and Mathe, V. L., "Structural, dielectric properties and AC conductivity of Ni$_{(1-x)}$Zn$_x$Fe$_2$O$_4$ spinel ferrites", *J. Alloys Compd.*, vol. 502, pp. 231-237, 2010.

[70]   Momin, A. A., Parvin, R., Islam, M. F., and Hossain, A. K. M. A., "Structural, magnetic and electrical properties of multiferroic xLi$_{0.1}$Ni$_{0.2}$Mn$_{0.6}$Fe$_{2.1}$O$_4$–(1-x)Bi$_{0.8}$Y$_{0.2}$FeO$_3$ composites", *J. Magn. Magn. Mater.*, 526, p. 167708, 2021.

[71]   Ren, X. M., Ma, B. Y., Zhang, Y. R., Zhu, Q., Li, D. X., Li, S.M., Yuan, L., Yu, J. K., Liu, G. Q., and Li, H. X., "Effects of sintering temperature and V$_2$O$_5$ additive on the properties of SiCAl$_2$O$_3$ ceramic foams", *J. Alloys Compd.,* vol. 732, pp. 716–724, 2018.

[72]   Wang, A. P., Su, H., Tang, X.L., Li, Y. X., Xu, Z. Q., and Jing, Y. L., "Comparison between Nb$_2$O$_5$ and CaCO$_3$ additions on the DC-bias-superposition characteristic of low-temperature- fired NiCuZn ferrites", *J. Mater. Sci. Mater. Electron.,* vol. 29, pp. 14605–14611, 2018.

[73]   Ribeiro, U. L., Nasar, R. S., Nasar, M. C., and de Araujo, J. H., "Liquid phase sintering of ferrite of NiCuZn with low magnetic permeability for miniaturization", *Ceram. Int.,* vol. 44 pp. 723–727, 2018.

[74]   Jin, Y., Zhu, H., Xu, Y., Jin, Y., and Xu, Z., "Effects of Bi$_2$O$_3$–WO$_3$ additive on microstructure and magnetic properties of low-temperature-fired MgCuZn ferrites," *J. Mater. Sci.: Mater. Electron.,* vol. 26, pp. 4325-4329, 2015.

[75] Yang, Y., Zhang, H., Li, J., Xu, F., Gan, G., and Wen, D., "Effects of Bi_2O_3-Nb_2O_5 additives on microstructure and magnetic properties of low-temperature-fired NiCuZn ferrite ceramics", *Ceram. Int.,* vol. 44, pp. 10545-10550, 2018.

[76] Yan, S., Liu, S., He, L., He, J., Huang, S., and Deng, L., "Investigation on microstructure and magnetic properties in V_2O_5 doped NiCuZn ferrite", *Mater. Res. Express.*, vol. 6, p. 076111, 2019.

[77] Smit, J., and Wijn, H. P.J., Ferrites, Philips technical library, Eindhoven, The Netherlands, vol. 278, 1959.

[78] Jain, G. C., Das, B. K., Tripathi, R. B., and Narayan, R., "Influence of V_2O_5 on the densification and the magnetic properties of Ni—Zn ferrite", *J. Magn. Magn. Mater.*, vol. 14, pp. 80-86, 1979.

[79] Haque, M. M., Huq, M., and Hakim, M. A., "Effect of Zn^{2+} substitution on the magnetic properties of $Mg_{1-x}Zn_xFe_2O_4$ ferrites", *Phys. Rev. B Condens. Matter.*, vol. 404, pp. 3915-3921, 2009.

[80] Hossain, M. D., Jamil, A. T. M. K., Hasan, M. R., Ali, M. A., Esha, I. N., Hossain, M. S., Hakim, M. A., and Khan, M. N. I., "Impact of V substitution on the physical properties of Ni–Zn–Co ferrites: structural, magnetic, dielectric and electrical properties", *Mater. Res. Express.*, vol. 8, p. 046102, 2021.

[81] Du, J., Yao, G., Liu, Y., Ma, J., and Zu, G., "Influence of V_2O_5 as an effective dopant on the sintering behavior and magnetic properties of $NiFe_2O_4$ ferrite ceramics", *Ceram. Int.,* vol. 38, pp. 1707-1711, 2012.

[82] Dimri, M. C., Verma, A., Kashyap, S. C., Dube, D. C., "Thakur, O. P. and Prakash, C., Structural, dielectric and magnetic properties of NiCuZn ferrite grown by citrate precursor method", *Mater. Sci. Eng. B*, vol. 133, pp. 42-48, 2006.

[83] Fu, Y. P., and Hu, S. H., "Electrical and magnetic properties of magnesium-substituted lithium ferrite", *Ceram. Int.*, vol. 36, pp. 1311-1317, 2010.

[84] Snoek, J. L., "Dispersion and absorption in magnetic ferrites at frequencies above one Mc/s", *Physica*, vol. 14, pp.207-217, 1948.

[85] Melagiriyappa, E., Jayanna, H. S., and Chougule, B.K., "Dielectric behavior and ac electrical conductivity study of Sm^{3+} substituted Mg–Zn ferrites", *Mater. Chem. Phys.*, vol. 112, pp. 68-73, 2008.

[86] Singh, N., Agarwal, A., and Sanghi, S., "Dielectric relaxation, conductivity behavior and magnetic properties of Mg substituted Zn–Li ferrites", *Curr. Appl. Phys.*, vol. 11, pp. 783-789, 2011.

[87] Verwey, E. J. W., and de Boer, J. H., "Cation arrangement in a few oxides with crystal structures of the spinel type", *Rec. Trav. Chim. Pays-Bas*, vol. 55, pp. 531–540, 1936.

[88] Iwauchi, K., "Dielectric properties of fine particles of Fe_3O_4 and some ferrites", *Jpn. J. Appl. Phys.*, vol. 10, p.1520, 1971.

[89] Uddin, M. F., Ullah, M. S., Hoque, S. M., Khan, F.A., Momin, A. A., Islam, Sm. R., Salehin, F. and Hakim, M. A., "Electrical transport properties of V_2O_5-added Ni–Co–Zn ferrites", *J. Adv. Dielectr.*, p.2150025, 2021.

[90] Dar, M. A., Batoo, K. M., Verma, V., Siddiqui, W. A., and Kotnala, R. K., "Synthesis and characterization of nano-sized pure and Al-doped lithium ferrite having high value of dielectric constant", *J. Alloys Compd.,* vol. 493, pp. 553-560, 2010.

[91] Jonscher, A. K., "The 'universal'dielectric response", *nature*, vol. 267, pp. 673-679, 1977.

[92] Kaiser, M., "Influence of V_2O_5 ion addition on the conductivity and grain growth Ni–Zn–Cu ferrites", *Curr. Appl. Phys.,* vol. 10, pp. 975-984, 2010.

[93] Macedo, P. B., PB, M., and CT, M., "The role of ionic diffusion in polarisation in vitreous ionic conductors", *Ceram. Int.* vol. 13, pp. 171–179, 1972.

[94] Rahaman, M. D., Setu, S. H., Saha, S. K., and Hossain, A. K. M. A., "Synthesis and characterization of $La_{0.75}Ca_{0.15}Sr_{0.05}Ba_{0.05}MnO_3–Ni_{0.9}Zn_{0.1}Fe_2O_4$ multiferroic composites", *J. Magn. Magn. Mater.,* vol. 385, pp. 418-427, 2015.

[95] Saha, S. K., Rahaman, M. D., Zubair, M. A., and Hossain, A. K. M. A., "Structural, electrical, magnetic and magnetoelectric properties of $(1-y)[Ba_{0.6-x}Ca_xSr_{0.4}Zr_{0.25}Ti_{0.75}O_3]$ + $(y)[(Li_{0.5}Fe_{0.5})_{0.4}Ni_{0.18}Cu_{0.12}Zn_{0.3}Fe_2O_4]$ composites", *J. Alloys Compd.*, 698, pp. 341-356, 2017.

Appendix

List of conference presentation

1. **Islam, Sm. R.,** Uddin, M. F., Satara, R., Hoque, S. M. and Ullah, M. S., "Complex permeability studies on Li-Zn ferrites: effect of V_2O_5 addition", Oral presentation, Sixth Conference (virtual) of Bangladesh Crystallographic Association, Venue: Zoom Online Platform, Date: 15-16 January 2021.

2. **Islam, Sm. R.,** Rahman, M. M., Hoque, S. M. and Ullah, M. S., "Dielectric properties and impedance spectroscopy of V_2O_5 added Li-Zn Ferrites", Oral presentation, National Conference on Physics-2021, Organized by Bangladesh Physical Society, Venue: Zoom Online Platform, Date: 06-07 August, 2021.

3. **Islam, Sm. R.,** Hoque, S. M., Khan, M. N. I., Khan, F. A., and Ullah, M. S., "Influence of V_2O_5 addition on the magnetic properties of Li-Zn ferrites", Poster presentation, International Conference on Electronics and Informatics 2021, Organized by Bangladesh Electronics and Informatics Society, Venue: Atomic Energy Centre, Dhaka, Date: 27-28 November, 2021.